Systematic study of temperature and density variations in effective potentials for coarse-grained models of molecular liquids

Kathryn M. Lebold[1] and W. G. Noid[1, a)]

Department of Chemistry, Penn State University, University Park, Pennsylvania 16802 USA

(Dated: May 14, 2020)

Due to their computational efficiency, coarse-grained (CG) models are widely adopted for modeling soft materials. As a consequence of averaging over atomistic details, the effective potentials that govern the CG degrees of freedom vary with temperature and density. This state-point dependence not only limits their range of validity, but also presents difficulties when modeling thermodynamic properties. In this work, we systematically examine the temperature- and density-dependence of effective potentials for 1-site CG models of liquid ethane and liquid methanol. We employ force-matching and self-consistent pressure-matching to determine pair potentials and volume potentials, respectively, that accurately approximate the many-body potential of mean force (PMF) at a range of temperatures and densities. The resulting CG models quite accurately reproduce the pair structure, pressure, and compressibility of corresponding AA models at each state point for which they have been parameterized. The calculated pair potentials vary quite linearly with temperature and density over the range of liquid state points near atmospheric pressure. These pair potentials become increasingly repulsive both with increasing temperature at constant density and also with increasing density at constant temperature. Interestingly, the density-dependence appears to dominate, as the pair potentials become increasingly attractive with increasing temperature at constant pressure. The calculated volume potentials determine an average pressure correction that also varies linearly with temperature, although the associated compressibility correction does not. The observed linearity allows for predictions of pair and volume potentials that quite accurately model these liquids in both the constant NVT and constant NPT ensembles across a fairly wide range of temperatures and densities. More generally, for a given CG configuration and density, the PMF will vary linearly with temperature over the temperature range for which the entropy associated with the conditioned distribution of atomic configurations remains constant.

[a)]Electronic mail: wnoid@chem.psu.edu

I. INTRODUCTION

By eliminating superfluous atomic details, coarse-grained (CG) models facilitate studies of phenomena that cannot be effectively simulated with atomistic models.[1–7] The potentials governing the interactions in a CG model necessarily reflect averaging over the atomistic structures and interactions that have been eliminated from the CG model. Because these averages depend upon the thermodynamic state point, the resulting effective potentials often demonstrate limited transferability, i.e., potentials that have been parameterized for a specific thermodynamic state point are not guaranteed to accurately describe other state points.[4,5] Moreover, the state-point dependence of effective potentials also leads to surprising difficulties for modeling thermodynamic properties,[8–14] which have been termed "representability" problems.[15,16] These difficulties are particularly significant for "bottom-up" coarse-graining approaches that determine effective potentials as approximations to the many-body potential of mean force (PMF), which is defined by formally integrating out atomic degrees of freedom.[1,17–19] In rare instances these effective potentials and their state-point dependence can be determined analytically.[20–24] Much more commonly, though, bottom-up approaches determine effective potentials via computational methods that do not explicitly account for their state-point dependence.[5]

Consequently, many studies have investigated the temperature-dependence of the effective potentials obtained from bottom-up approaches. For instance, prior studies have optimized potentials for a single temperature and then examined the temperature range of their validity for complex liquids and polymers.[25–32] One can imagine employing a variational principle[33] or multistate iterative Boltzmann inversion[34] to determine a single temperature-independent potential that provides an optimal compromise over a specified temperature range. Other studies have characterized trends in the effective potentials optimized for specific temperatures.[16,35–40] Based upon the observed trends, as well as theoretical analysis, studies have proposed various functional forms for modeling this temperature dependence.[38–43] Similarly, several studies have employed temperature-dependent dielectric constants for treating electrostatic interactions in CG models.[44–46] It is also interesting that several recent "top-down" models have adopted temperature-dependent Lennard-Jones parameters to more accurately describe dynamical or thermodynamic properties.[47–49]

Many studies have also investigated the density-dependence of effective potentials. For

instance, recent studies have examined the importance of density for effective potentials derived from cluster expansion methods[50] and from integral equation theories.[51] Prior studies have examined the effects of solute concentration upon effective interactions in implicit solvent CG models for solutions of small molecules, polymers, and colloids.[1,39,52–56] Similarly, several studies have investigated the concentration-dependence of ionic interactions in implicit solvent CG models.[45,57–59] Moreover, effective pair potentials for CG water models also vary significantly with density.[16,37] These considerations have motivated more complex potentials that depend upon the local environment.[60–68]

Nevertheless, despite this considerable body of prior work, there exist few practical guidelines for either qualitatively understanding or quantitatively predicting the state-point dependence of effective potentials for specific molecular systems. Consequently, in this work we systematically examine the state-point dependence of effective potentials and, more specifically, the many-body PMF for CG models of molecular liquids. In particular, we employ the multiscale coarse-graining (MS-CG) method[69,70] to determine effective pair potentials that optimally approximate the configuration-dependence of the many-body PMF at each state point of interest.[71,72] The MS-CG method determines these potentials directly from the underlying atomic ensemble. In contrast, iterative coarse-graining methods, such as iterative Boltzmann inversion[73] or the Inverse Monte Carlo method,[74] can suffer from practical convergence issues[29,34,75] that may obscure the state-point dependence of the many-body PMF.

We consider 1-site CG models for liquid ethane and methanol. These are very simple systems and rather uninteresting per se, but they present several advantages for examining the state-point dependence of effective potentials. First of all, although ethane and methanol lack significant conformational flexibility, the CG model averages over not only vibrational fluctuations, but also important rotational degrees of freedom. Moreover, the 1-site representation eliminates the need to accurately describe the coupling between intra- and inter-molecular degrees of freedom in the CG model. Consequently, the MS-CG variational principle determines pair potentials that provide a very accurate approximation for the configuration-dependence of the many-body PMF at each state point.[76,77] Furthermore, the generalized-Yvon-Born-Green (g-YBG) theory[78,79] provides a particularly transparent framework for understanding the relationship between the MS-CG pair potential and the pair potential of mean force (pmf) that is determined by the radial distribution function,

as well as for understanding the many-body correlations that are relevant for the accuracy of the CG model.[80] Finally, although ethane and methanol have similar shapes, their interactions demonstrate rather different character. Thus, we can distinguish aspects of the CG potentials that reflect specific hydrogen-bonding interactions present in methanol from the aspects that reflect non-specific van der Waals-type interactions present in both systems.

We first examine the temperature-dependence of the MS-CG pair potentials at constant density before examining their density-dependence at constant temperature. We also examine the state-point dependence of the volume potential that determines corrections to the pressure and compressibility that are necessary for accurately modeling the volume-dependence of the many-body PMF.[81–83] We observe that the calculated pair potentials vary quite linearly with temperature and density for state points that correspond to liquids near 1 bar external pressure. Over this range of state points, the pair potentials become increasingly repulsive with increasing temperature at constant density, as well as with increasing density at constant temperature. Interestingly, the density-dependence appears more significant under these conditions, as the pair potentials become increasingly attractive with increasing temperature at constant pressure. Accordingly, the pressure correction linearly decreases with increasing temperature, although it remains very large ($> 10^3$ bar) even near the boiling point. We also observe that the pair pmf and the MS-CG pair potentials vary quite differently with temperature, which we examine with the g-YBG theory. Finally, we demonstrate that the pair potentials and pressure corrections can be quite accurately predicted for modeling other liquid phase state points near atmospheric pressure in either the constant NVT or constant NPT ensemble.

The remainder of this paper is organized as follows. Section II reviews the basic theory that is relevant for the state-point dependence of effective potentials. Sections III and IV describe the details and results of our calculations, respectively. Section V summarizes these results, discusses their significance, and also provides closing comments.

II. THEORY

A. Exact coarse-graining

We consider an atomistic model governed by a potential $u(\mathbf{r})$ where $\mathbf{r} = (\mathbf{r}_1, \ldots, \mathbf{r}_n)$ specifies the configuration for n atoms. The probability for sampling $\mathbf{r}$ at constant volume, V, and temperature, T, is

$$p_r(\mathbf{r}; V, T) = \exp\left[-\beta u(\mathbf{r})\right] / z(V, T) \tag{1}$$

where $\beta = 1/k_B T$ and z is the configuration integral.[84]

We consider a CG model that represents the same system with N sites. We assume a mapping, $\mathbf{M} = (\mathbf{M}_1, \ldots, \mathbf{M}_N)$, that specifies the configuration, $\mathbf{R} = (\mathbf{R}_1, \ldots, \mathbf{R}_N)$, of the N sites as a linear function of atomic coordinates:

$$\mathbf{M}_I(\mathbf{r}) = \sum_i c_{Ii} \mathbf{r}_i \quad \text{for each } I = 1, \ldots, N \tag{2}$$

where the mapping coefficients, c_{Ii} are non-negative and normalized such that $\sum_i c_{Ii} = 1$ for each I.[72] Additionally, we assume that each atom is associated with at most one CG site.

The central quantity in bottom-up coarse-graining is the effective potential[1,5,8,17,18]

$$\exp\left[-\beta W_N(\mathbf{R}, V; T)\right] = \omega_N(\mathbf{R}, V)^{-1} \int_{V^n} \mathrm{d}\mathbf{r}\, \exp\left[-\beta u(\mathbf{r})\right] \delta(\mathbf{M}(\mathbf{r}) - \mathbf{R}), \tag{3}$$

where

$$\omega_N(\mathbf{R}, V) \equiv \int_{V^n} \mathrm{d}\mathbf{r}\, \delta(\mathbf{M}(\mathbf{r}) - \mathbf{R}) = V^{n-N} \tag{4}$$

is the volume element of atomic configuration space that maps to $\mathbf{R}$.[24] Here we assume that configuration space is homogeneous, e.g., due to periodic boundary conditions, such that ω_N is independent of $\mathbf{R}$. The probability that the atomistic model samples a configuration $\mathbf{r}$ that maps to $\mathbf{R}$ is

$$p_R(\mathbf{R}; V, T) \equiv \int_{V^n} \mathrm{d}\mathbf{r}\, p_r(\mathbf{r}; V, T) \delta(\mathbf{M}(\mathbf{r}) - \mathbf{R}) = V^{n-N} \exp\left[-\beta W_N(\mathbf{R}, V; T)\right] / z(V, T). \tag{5}$$

Consequently, $W_N(\mathbf{R}, V; T)$ is the appropriate potential for properly sampling the CG configuration space at a given V and T.[72] Moreover, because

$$V^{-N} \int_{V^N} \mathrm{d}\mathbf{R}\, \exp\left[-\beta W_N(\mathbf{R}, V; T)\right] = V^{-n} \int_{V^n} \mathrm{d}\mathbf{r}\, \exp\left[-\beta u(\mathbf{r})\right], \tag{6}$$

$W_N(\mathbf{R}, V; T)$ preserves the excess thermodynamic properties of the atomic model.[14] As expected for a thermodynamic potential, W_N may be decomposed into energetic and entropic contributions[24]

$$W_N(\mathbf{R}, V; T) = U_W(\mathbf{R}, V; T) - TS_W(\mathbf{R}, V; T). \tag{7}$$

The energetic contribution is a conditioned canonical average of the atomic potential,

$$U_W(\mathbf{R}, V; T) \equiv \langle u(\mathbf{r}) \rangle_{\mathbf{R};V,T} \tag{8}$$

where the subscripted angular brackets denote an average according to

$$p_{r|R}(\mathbf{r}|\mathbf{R}; V, T) \equiv p_r(\mathbf{r}; V, T)\delta(\mathbf{M}(\mathbf{r}) - \mathbf{R}) / p_R(\mathbf{R}; V, T). \tag{9}$$

The entropic contribution, S_W, incorporates into W_N the excess configurational entropy associated with the distribution of atomic configurations that map to a given CG configuration:

$$S_W(\mathbf{R}, V; T) \equiv \left\langle -k_B \ln \left[\frac{p_{r|R}(\mathbf{r}|\mathbf{R}; V, T)}{q_{r|R}(\mathbf{r}|\mathbf{R}; V, T)} \right] \right\rangle_{\mathbf{R};V,T} \leq 0 \tag{10}$$

where

$$q_{r|R}(\mathbf{r}|\mathbf{R}; V, T) \equiv \delta(\mathbf{M}(\mathbf{r}) - \mathbf{R}) / \omega_N(\mathbf{R}, V) \tag{11}$$

is the uniform conditional probability distribution.[24] The total differential of W_N is

$$\mathrm{d}W_N = -\sum_I \overline{\mathbf{f}}_I \cdot (\mathrm{d}\mathbf{R}_I)_V - \overline{p}_{\mathrm{xs}} \mathrm{d}V - S_W \mathrm{d}T, \tag{12}$$

where we have suppressed the arguments for simplicity.[14] Here $(\mathrm{d}\mathbf{R}_I)_V$ denotes the variation in each site coordinate at constant V, i.e., $(\mathrm{d}\mathbf{R}_I)_V \equiv V^{1/3}\mathrm{d}\hat{\mathbf{R}}_I$ where $\hat{\mathbf{R}}_I \equiv V^{-1/3}\mathbf{R}_I$ is the scaled CG coordinate,

$$\overline{\mathbf{f}}_I(\mathbf{R}; V, T) \equiv \langle \mathbf{f}_I(\mathbf{r}) \rangle_{\mathbf{R};V,T} \tag{13}$$

is the conditioned average of the net force on site I, such that W_N is a potential of mean force,[1,72,85] and

$$\overline{p}_{\mathrm{xs}}(\mathbf{R}, V; T) \equiv \langle p_{\mathrm{xs}}(\mathbf{r}, V) \rangle_{\mathbf{R};V,T} \tag{14}$$

is the conditioned average of the atomic excess pressure $p_{\mathrm{xs}}(\mathbf{r}, V) = -(\partial u/\partial V)_{\hat{\mathbf{r}}}$, where the partial derivative is evaluated at fixed scaled atomic coordinates, $\hat{\mathbf{r}} = V^{-1/3}\mathbf{r}$.[81,82] Importantly, Eq. (12) demonstrates that the derivatives of W_N with respect to temperature and volume equal the atomic contributions to the corresponding thermodynamic properties

that have been transferred from the atomic configuration space into the effective potential.[14] Thus, if one could accurately determine S_W and $\overline{p}_{\rm xs}$, then one could both predict the state-point dependence of W_N and also account for the atomic contributions to the entropy and pressure. Note that if $p_{r|R}$ is independent of temperature for some $\mathbf{R}$, then S_W will also be independent of temperature and W_N will vary linearly with T for this CG configuration.

B. Approximate coarse-graining

We seek to investigate the state-point dependence of W_N. Unfortunately, Eqs. (3), (8), and (10) are not computationally tractable. However, Eqs. (12)-(14) provide computationally feasible means for characterizing variations in W_N via variational principles expressed in terms of mechanical variables, such as forces and pressures.

Accordingly, we approximate W_N with the potential,

$$U(\mathbf{R}, V) = U_R(\mathbf{R}) + U_V(V) \tag{15}$$

where the interaction potential, U_R, is an explicit function of only the configuration, while the volume potential, U_V, is independent of configuration.[81,82] We optimize the interaction potential in order to approximate the configuration dependence of W_N by adopting the MS-CG force-matching variational principle[69,70,72,86] and minimizing

$$\chi_1^2[U_R] = \left\langle \frac{1}{3N} \sum_I \left| \mathbf{f}_I(\mathbf{r}) - \mathbf{F}_I(\mathbf{M}(\mathbf{r})) \right|^2 \right\rangle \tag{16}$$

where $\mathbf{F}_I = -\partial U_R / \partial \mathbf{R}_I$ and the angular brackets denote ensemble averages evaluated for the atomic model at either constant volume or constant external pressure. Note that, because it is expressed in terms of forces, χ_1^2 is insensitive to aspects of W_N that vary with thermodynamic state point but are independent of, or vary only slowly with, changes in configuration. Consequently, given U_R, Das and Andersen proposed determining U_V such that $U = U_R + U_V$ optimally approximates the volume-dependence of W_N.[81] Specifically, Das and Andersen proposed a pressure-matching variational principle for determining U_V by minimizing

$$\chi_2^2[U_V|U_R] = \left\langle \left| \Delta P_{\rm id}(V) + p_{\rm xs}(\mathbf{r}, V) - P_{\rm xs}(\mathbf{M}(\mathbf{r}), V) \right|^2 \right\rangle \tag{17}$$

where $\Delta P_{\rm id}(V) = (n-N)k_BT/V$ is the difference in the ideal contribution to the atomic and CG pressures, while $P_{\rm xs} = -\left(\partial U / \partial V\right)_{\hat{\mathbf{R}}} = -\left(\partial U_R / \partial V\right)_{\hat{\mathbf{R}}} - \mathrm{d}U_V/\mathrm{d}V$. Dunn and Noid later

proposed a self-consistent pressure-matching variational principle that iteratively refines U_V in order to more accurately model the volume-dependence of W_N.[82] This corresponds to optimizing U_V by minimizing a relative entropy[83,87,88]

$$S_{\rm rel}[U_V|U_R] = \int \mathrm{d}V \int_{V^N} \mathrm{d}\mathbf{R}\, p_{RV}(\mathbf{R},V) \ln\left[\frac{p_{RV}(\mathbf{R},V)}{P_{RV}(\mathbf{R},V;U_V|U_R)}\right], \tag{18}$$

where p_{RV} and P_{RV} are probability distributions for the atomic and CG models to sample the configuration $\mathbf{R}$ and volume V in the constant NPT ensemble.[83]

C. Pair structure

In the present work we consider the particularly simple case that each molecule is represented by a single site and U_R is pair additive:

$$U_R(\mathbf{R}) = \sum_{(I,J)} U_2(R_{IJ}), \tag{19}$$

where the sum is performed over all distinct pairs, (I,J), of sites and $R_{IJ} = |\mathbf{R}_I - \mathbf{R}_J|$ is the distance between the pair. In this case, a particularly useful characteristic of the liquid structure is given by the pair correlation function[84]

$$g_2(\mathbf{R}_1,\mathbf{R}_2) = \rho^{-2}\rho_2(\mathbf{R}_1,\mathbf{R}_2), \tag{20}$$

where $\rho = N/V$ is the density of molecules and $\rho_2(\mathbf{R}_1,\mathbf{R}_2)$ is the probability density that any two molecules (or, more precisely, any two CG sites) are at positions $\mathbf{R}_1$ and $\mathbf{R}_2$. In the limit that $N^{-1} \to 0$, the pair correlation function may be expressed

$$g_2(\mathbf{R}_1,\mathbf{R}_2) = \exp\left[-\beta\left(W_2(\mathbf{R}_1,\mathbf{R}_2) - A_{\rm xs}\right)\right] \tag{21}$$

where we define

$$\exp\left[-\beta A_{\rm xs}\right] = \omega_0^{-1}\int_{V^n} \mathrm{d}\mathbf{r}\, \exp\left[-\beta u(\mathbf{r})\right] \tag{22}$$

$$\exp\left[-\beta W_2(\mathbf{R}_1,\mathbf{R}_2)\right] = \omega_2^{-1}\int_{V^n} \mathrm{d}\mathbf{r}\, \exp\left[-\beta u(\mathbf{r})\right] \delta(\mathbf{R}_1 - \mathbf{M}_1(\mathbf{r}))\, \delta(\mathbf{R}_2 - \mathbf{M}_2(\mathbf{r})) \tag{23}$$

as free energy functions of the form given by Eq. (3), while $\omega_0 = V^n$ and $\omega_2 = V^{n-2}$ are corresponding volume elements. Thus, while W_2 and $A_{\rm xs}$ both systematically increase with temperature, the conventional pair potential of mean force (pmf)

$$w_2(\mathbf{R}_1,\mathbf{R}_2) \equiv -k_B T \ln g_2(\mathbf{R}_1,\mathbf{R}_2) = W_2(\mathbf{R}_1,\mathbf{R}_2) - A_{\rm xs} \tag{24}$$

does not necessarily increase with temperature. For the cases of homogeneous isotropic liquids that we consider here, $g_2(\mathbf{R}_1, \mathbf{R}_2) = g(R_{12})$ is the radial distribution function (rdf) and $w_2(\mathbf{R}_1, \mathbf{R}_2) = w_2(R_{12})$.[84]

The MS-CG pair potentials, U_2, that minimize χ_1^2 satisfy a generalized-Yvon-Born-Green (g-YBG) equation[71,77,78,89]

$$-\,\mathrm{d}w_2(R)/\mathrm{d}R = F_2(R) + \int \mathrm{d}R' K(R, R') F_2(R'). \tag{25}$$

In this equation, $-\mathrm{d}w_2(R)/\mathrm{d}R$ is the pair mean force, i.e., the average net force experienced by a central particle when a second particle is a distance R away,[17,90] $F_2(R) = -\mathrm{d}U_2(R)/\mathrm{d}R$ is the MS-CG pair force function, and

$$K(R, R') = \frac{1}{cR^2 g(R)} \left\langle \sum_{\lambda}^{\text{triples}} \cos\theta_\lambda \, \delta(R_{\lambda J} - R) \, \delta(R_{\lambda K} - R') \right\rangle \tag{26}$$

quantifies three-body correlations in terms of the angle θ_λ formed by each pair, $\{J, K\}$, of particles around each central particle, λ, as a function of the distances R and R' from the pair to the central particle.[80] Thus, according to Eq. (25), the MS-CG method determines the optimal pair potential by first decomposing the pair mean force into direct and indirect contributions and then assigning the direct contribution to the MS-CG pair potential. This provides a direct relation between the pair structure in the atomic model, as quantified by the rdf, and the MS-CG pair potential.

III. METHODS

A. AA model and simulations

We performed all-atom (AA) simulations of 1-component systems of liquid ethane and liquid methanol in both the constant NVT and constant NPT ensembles. We performed all atomistic simulations with GROMACS version 4.5.3[91] with three-dimensional periodic boundary conditions. We did not rigidly constrain any bonds and employed a 1 fs time step to propagate dynamics. We modeled all atomistic interactions with the OPLS-AA force field,[92] while switching Lennard-Jones potentials to zero between 1.2 and 1.4 nm. We accounted for this truncation by employing corresponding dispersion corrections to the energy and pressure. We modeled electrostatic interactions with the Particle-Mesh-Ewald method,[93] while adopting a real-space cutoff of 1.4 nm and a grid spacing of 0.08 nm.

Table I summarizes the simulated state points. Simulations of ethane and methanol employed 793 and 953 molecules, respectively. We employed the stochastic dynamics integrator with an inverse friction constant of 0.1 ps to control the temperature of each simulation.[94] We performed all constant NVT simulations in a fixed cubic box with 4 nm sides. We performed constant NPT simulations at 1 bar external pressure by also employing the Parrinello-Rahman barostat[95] with a time constant of 5.0 ps and compressibility of 4.5×10^{-5} bar^{-1}.

We simulated a set of temperatures that span in increments of 25 K the temperature range over which the system is liquid at atmospheric pressure. We constructed an initial configuration for each temperature by first placing the molecules on a lattice in a cubic box with 4 nm sides. We then annealed and equilibrated the system for each target temperature at constant volume. Briefly, after minimizing the energy of the lattice configuration, we annealed the system temperature to 1000 K over the course of 3 ns and then simulated at 1000 K for 2 ns. Starting from this high temperature configuration, we annealed copies of the system to each target temperature over the course of 3 ns and then equilibrated the system at constant temperature for 2 ns. The final configuration from this equilibration served as the initial configuration for 10 ns production simulations in both the constant NVT and constant NPT ensembles. In the case of the constant NPT simulation, we discarded the first 0.2 ns of this simulation as an additional equilibration period. We sampled configurations from the production simulations after each picosecond.

We estimated the pressure equation of state from NPT simulations by discretizing the sampled volume range into bins centered around specific volumes. We determined the average pressure at each discrete volume from the mean of the instantaneous internal pressures sampled in the corresponding bin. For both NVT and NPT simulations, we determined the statistical uncertainty in mean pressures from the standard error: Given $N_p \gg 1$ samples for the internal pressure, which are assumed statistically independent, we determined the statistical uncertainty by $\delta P = \sigma_P / N_p^{1/2}$, where σ_P is the standard deviation in the N_p samples.

B. CG model and simulations

We parameterized a specific CG model for each system in each state point of interest. While some studies have employed higher resolution representations for methanol,[33,70,96,97]

we represented both molecules with a single spherical site corresponding to the mass center. In each case, we approximated the corresponding many-body PMF, W_N, with the potential, $U = U_R + U_V$, of Eq. (15). The interaction potential, U_R, consisted of short-ranged central pair potentials according to Eq. (19). We represented the volume potential

$$U_V(V) = N\left\{\psi_1 V/\overline{v} + \psi_2 \left(V/\overline{v} - 1\right)^2\right\}, \tag{27}$$

where ψ_1 and ψ_2 are parameters optimized for each atomic ensemble, $\overline{v}$ is the average volume of this ensemble, and N is the number of molecules.[81,82]

We parameterized these models with the bottom-up open-source coarse-graining software (BOCS) package version 1.0, which is freely available online at `https://github.com/noid-group/BOCS` and has been recently discussed in detail.[98] In brief, we first mapped each AA trajectory to its CG representation. We then determined the optimal pair potentials by solving the normal system of linear equations that minimize χ_1^2 in Eq. (16).[71,72] We performed these force-matching calculations with the $v^{2/3}$ reweighting previously suggested by Das and Andersen,[81] although our prior studies suggest that this reweighting has little significance in practice.[82,83,98] In this calculation, we represented the pair potentials with cubic spline basis functions with a grid spacing of 0.02 nm, while truncating the potentials at 1.4 nm and smoothly extrapolating the calculated potentials into the hard core region. We then optimized the parameters for the volume potential in Eq. (27) via iterative pressure-matching.[82,83,98] This optimization required fewer than 4 iterations to determine volume potentials that accurately reproduced the corresponding atomic density fluctuations for each temperature at 1 bar external pressure.

We simulated the CG model in the constant NVT ensemble with the Gromacs 4.5.3 package, while employing the same parameters described above for the atomistic simulations. We simulated the CG model in the constant NPT ensemble with a modified version[98] of the LAMMPS package[99] that accounts for the pressure correction due to U_V in the Martyna-Tuckerman-Tobias-Klein (MTTK) volume equation of motion.[100,101] These LAMMPS simulations employed the velocity verlet algorithm to propagate dynamics with a 1.0 fs timestep, while employing the modified MTTK barostat with a relaxation time of 1.0 ps to control the pressure and a Nosé-Hoover chain[102] of length three with a relaxation time of 0.1 ps to control the temperature. We obtained an initial configuration for each CG simulation by mapping to the CG resolution the final frame of the corresponding atomistic simulation.

IV. RESULTS

In this section we analyze the sensitivity of CG structure and interactions to changes in the thermodynamic state. Specifically, we consider 1-site MS-CG models of liquid ethane and methanol that represent each molecule with its mass center. In order to investigate the effect of varying temperature at fixed volume, we first consider simulations that sample the canonical ensemble at different temperatures, but with the same fixed density. In order to investigate the effect of varying density, we then consider simulations that sample the isothermal-isobaric ensemble at different temperatures, but a single fixed external pressure of 1.0 bar. Table I summarizes the simulated state points. Although this is not our primary focus, the Supporting Information (SI) demonstrates that the MS-CG models accurately describe the atomic pair structure and pressure-volume equation of state for each state point considered.

A. Ethane

Figure 1 characterizes the pair structure and effective interactions generated by atomically detailed simulations of ethane that sample the constant NVT ensemble with a density $\rho_0 = 618.7$ g/L. In Figs. 1-6(a), the black, red, green, and blue curves present results for simulations at $T = 100$ K, 125 K, 150 K, and 175 K, respectively.

Figure 1(a) presents the radial distribution functions (rdfs) obtained by mapping the atomistic simulations to the 1-site CG representation. The rdfs feature a broad first peak with a maximum at $r \approx 0.45$ nm and a shoulder at $r \approx 0.51$ nm, which correspond to adjacent molecules aligned in parallel and in perpendicular fashions, respectively. The periodic oscillations in the rdf suggest that well-defined solvation shells exist out to 1.25 nm. The first peak of the rdf very slightly decreases with increasing temperature. Nevertheless, the ethane rdf appears essentially temperature-independent, suggesting that the structure of liquid ethane is similar to the athermal packing of hard dumbbells.

Figure 1(b) presents the pair potential of mean force (pmf), $w_2(r) = -k_B T \ln g(r)$. The features of the pair pmf, such as the contact minimum and desolvation barrier, clearly mirror the features of the rdf. Because the rdf is essentially temperature-independent, the pair pmf varies linearly with temperature. In particular, increasing temperature causes each minimum

to deepen and each barrier to rise.

Figure 1(c) presents the corresponding MS-CG pair potential, U_2, which corresponds to an optimal pair-additive decomposition of the many-body PMF, W_N. The MS-CG pair potential is strikingly different from the pair pmf. While w_2 demonstrates shallow oscillations corresponding to the peaks and troughs of the rdf, U_2 is much larger and almost purely repulsive. Moreover, U_2 is much shorter ranged and essentially vanishes beyond the first minimum of the rdf. Finally, in contrast to w_2, U_2 systematically increases with temperature at each distance. This suggests that the temperature-variation of the MS-CG interaction potential, $U_R(\mathbf{R}) = \sum_{(I,J)} U_2(R_{IJ})$, mimics the temperature-variation in the configuration-dependence of the many-body PMF, since Eq. (12) indicates that $(\partial W_N/\partial T)_{\mathbf{R};V} > 0$ in each configuration, $\mathbf{R}$.

Figure 1(d) presents the difference, $w_{\text{ind}} = w_2 - U_2$, between the pair pmf and the MS-CG pair potential. The (negative) derivative of the pmf gives the pair mean force, which is the conditioned average force on a central molecule when a second molecule is a distance r away. This pair mean force can be decomposed into a direct contribution from the second molecule, as well as an indirect, or solvation, contribution from the surrounding N-2 molecules. The g-YBG equation, Eq. (25), indicates that U_2 can be interpreted as the direct contribution to w_2. Consequently, w_{ind} can be interpreted as the indirect contribution to the pair pmf. This indirect contribution is relatively large and generally cancels the direct force. Importantly, w_{ind} is attractive over the first solvation shell and, thus, is solely responsible for the contact minimum of the pair pmf. Moreover, this term becomes increasingly attractive with increasing temperature, giving rise to the corresponding deepening of the contact minimum of the pair pmf.

The g-YBG theory also further clarifies the physical origin of w_{ind}.[80] According to Eq. (25), $-\mathrm{d}w_{\text{ind}}/\mathrm{d}r$ equals the conditioned mean force experienced by the central molecule due to interacting via the MS-CG pair potentials with the surrounding $N-2$ particles. Figure 2(a) illustrates the geometry of these solvation forces on the central molecule when a second molecule is separated by a distance r and one of the surrounding $N-2$ molecules is separated by a distance r'. Figure 2(b) presents an intensity plot of the matrix $K(r, r')$, which encodes the structural effects that determine these solvation forces.[71,77,80] In particular, the negative band for $r \approx r'$ reflects steric effects between pairs of particles in the same solvation shell of the central molecule, while the alternating bands parallel to the diagonal reflect successive

solvation shells of the central molecule. Since the MS-CG pair force becomes negligible for $r' \geq 0.65$ nm, $w_{\text{ind}}(r)$ primarily reflects the MS-CG pair force from surrounding molecules that are 0.35 nm $\leq r' \leq 0.65$ nm from the central molecule, i.e., from surrounding molecules that are in the first solvation shell of the central molecule. Over this range, the MS-CG pair force is repulsive (positive) while $K(r, r')$ is almost always negative. For this reason, w_{ind} generates a net attractive force between the pair due to repulsive interactions with the surrounding molecules.

Figure 3 quantifies the temperature variation of w_2, U_2, and w_{ind}. We estimate the temperature derivative of each potential, $(\partial U/\partial T)_{r,\rho}$, according to the finite difference:

$$\partial_T U(r; T, \rho_0) = \frac{U(r; T, \rho_0) - U(r; T_0, \rho_0)}{T - T_0} \tag{28}$$

where $U(r; T, \rho)$ indicates the potential determined from constant NVT simulations at the state point (T, ρ), $T_0 = 150$ K, and $\rho_0 = 618.7$ g/L. The dashed cyan curve presents the simple mean of the calculated finite differences.

Because the rdf is temperature independent, $\partial_T w_2$ is simply $-k_B \ln g(r)$, which is small and oscillates about zero except when $r \to 0$. The MS-CG pair potential, U_2, and the indirect contribution, w_{ind}, to the pair pmf also vary quite linearly with temperature. In particular, the temperature variation, $\partial_T U_2$, in the MS-CG potential is positive at almost all distances, achieves a maximum at contact, systematically decreases with increasing distance, and essentially vanishes for $r \geq 0.65$ nm. Because U_2 and w_{ind} vary in the opposite directions with increasing temperature, the pair pmf demonstrates considerably less temperature dependence. In principle, the temperature dependence of w_{ind} reflects changes in both the surrounding many-body structure, which is quantified by $K(r, r')$ in Fig. 2(b), as well as changes in the direct interaction between molecules, which is quantified by U_2. In particular, the dotted curve in Fig. 3(c) presents the contribution to $\partial_T w_{\text{ind}}$ that is due to the temperature-dependence of $K(r, r')$. Clearly, this contribution is negligible. Thus, it is interesting that, although the pair and three-body structure of liquid ethane vary little with temperature, the MS-CG pair potential significantly varies with temperature.

While Figures 1-3 consider temperature variations at constant density, Figure 4 considers the same temperature variations at a constant external pressure $P_0 = 1$ bar. As the temperature increases from 100 K to 175 K at atmospheric pressure, the simulated density decreased by 16%, as indicated in Table I.

Figure 4(a) presents the rdfs obtained by mapping atomically detailed constant NPT simulations to the CG representation. The rdfs obtained from constant NPT and constant NVT simulations are qualitatively similar. However, the rdfs obtained from constant NPT simulations demonstrate much greater variation with increasing temperature. In particular, the first peak decreases more significantly with increasing temperature at constant external pressure. Moreover, the constant NPT rdfs systematically shift to larger distances as the liquid expands with increasing temperature at constant external pressure.

Figure 4(b) presents the corresponding pair pmfs. With increasing temperature, the contact minimum deepens to a similar extent at both constant density and constant pressure. However, in contrast to the constant NVT pair pmfs, the constant NPT pair pmfs shift to larger distances with increasing temperature.

Figure 4(c) presents the MS-CG pair potentials calculated from these constant NPT simulations. These MS-CG potentials are qualitatively similar to the corresponding potentials calculated from the NVT simulations, as they are almost purely repulsive and are negligible for $r \geq 0.65$ nm. However, there is one striking difference: While the MS-CG pair potentials increased with temperature when calculated at constant density, they decrease with temperature when calculated at constant pressure. Indeed, by $T = 175$ K, the MS-CG pair potential includes a noticeable attractive well at $r \approx 0.5$ nm. Consequently, the pair pmfs and MS-CG pair potentials shift in opposite directions with increasing temperature at constant pressure. Since Fig. 1 indicates that the MS-CG potentials become more repulsive with increasing temperature at constant density, this opposite trend in Fig. 4(c) reflects the density-dependence of the pair potentials.

We quantified this density dependence by estimating the partial derivative $(\partial U/\partial \rho)_{r,T}$ according to the finite difference:

$$\partial_\rho U(r;T,\rho_T) = \frac{U(r;T,\rho_T) - U(r;T,\rho_0)}{\rho_T - \rho_0} \tag{29}$$

where $\rho_T = \rho(T, P_0)$ is the equilibrium density at temperature T and external pressure $P_0 = 1$ bar. In Eq. (29), $U(r;T,\rho_T)$ is the pair potential determined from constant NPT simulations at temperature T with the equilibrium density ρ_T, while $U(r;T,\rho_0)$ is the pair potential determined from constant NVT simulations at the same temperature and the fixed density ρ_0. Figure 5(a) presents the finite differences calculated for the NPT ensemble at each temperature, while the cyan curve presents a simple average of these finite differences.

The density derivatives are almost everywhere positive. Density increases primarily increase the short-ranged repulsion and have negligible effect upon the pair potential for $r \geq 0.65$ nm. Figure 5(a) also demonstrates that the MS-CG pair potentials vary approximately linearly with density over this range, although $\partial_\rho U$ slightly decreases with increasing temperature. Note that the marked differences observed in the finite differences for $r \leq 0.35$ nm correspond to short distances that are well into the hard-core region of the MS-CG potential. Consequently, these discrepancies reflect both poor statistics and also the fine details of the procedure used for extrapolating the calculated potentials into the hard-core region as $r \to 0$.

Figure 5(b) compares the MS-CG pair potentials calculated in the constant NPT ensemble at each temperature with potentials obtained by linear extrapolation from a single MS-CG pair potential, $U(r; T_0, \rho_0)$, calculated for the constant NVT ensemble at $T_0 = 150$ K and $\rho_0 = 618.7$ g/L:

$$U_{\text{lin}}(r; T, \rho_T) \equiv U(r; T_0, \rho_0) + \partial_T \bar{U}(r) \Delta T + \partial_\rho \bar{U}(r) \Delta\rho \tag{30}$$

where $\Delta T = T - T_0$ and $\Delta\rho = \rho_T - \rho_0$. In Eq. (30), $\partial_T \overline{U}(r)$ is the mean estimate for $(\partial U/\partial T)_{r,\rho}$ determined from constant NVT simulations according to Eq. (28), i.e., the cyan curve in Fig. 3(b), while $\partial_\rho \overline{U}(r)$ is the mean estimate for $(\partial U/\partial \rho)_{r,T}$ determined from constant NPT simulations according to Eq. (29), i.e., the cyan curve in Fig. 5(a). The linear extrapolations agree almost quantitatively with the constant NPT MS-CG potentials calculated at $T = 100$ K, 125 K, and 150 K. The extrapolation also qualitatively agrees with the constant NPT MS-CG potentials calculated at $T = 175$ K, although in this case it overestimates the depth of the attractive well. Nevertheless, these results indicate that the MS-CG potentials for the 1-site ethane model vary quite linearly over a relatively wide range of densities and temperatures.

The preceding figures examine the sensitivity of the MS-CG pair potentials to variations in temperature and density. While the force-matching variational principle determines pair potentials, U_2, that quite accurately approximate the configuration-dependence of the many-body PMF, force-matching and other structure-based approaches are much less sensitive to the volume-dependence of the PMF.[12,14,62] However, this volume-dependence must be accurately approximated in order to reproduce the atomic pressure.[14,81] Indeed, structure-based pair potentials typically overestimate the atomistic pressure by several or-

ders of magnitude.[10,12] Consequently, we introduce an additional term to the total potential, U_V, in order to accurately model the density-dependence of the many-body PMF:[81,82]

$$U_V(V) = N\left\{\psi_1 V/\overline{v} + \psi_2 \left(V/\overline{v} - 1\right)^2\right\},$$

where $\overline{v}$ is the average atomic volume, while ψ_1 and ψ_2 are parameters that we optimized via self-consistent pressure-matching.[82,83] The resulting "volume force" $F_V(V) = -\mathrm{d}U_V(V)/\mathrm{d}V$ then determines a correction to the pressure of the CG model that compensates for the highly repulsive pair potentials. In particular, ψ_1 is proportional to the average pressure correction, while ψ_2 specifies the correction to the compressibility of the CG model.

Figure 6(a) presents the pressure corrections, $F_V(V)$, that are necessary to reproduce the pressure-volume equation of state for the atomistic ethane model in the constant NPT ensemble at an external pressure $P_0 = 1$ bar. A pressure correction of nearly -7 kbar is necessary to match the volume dependence of the many-body PMF at relatively high densities near the freezing point. Successively smaller pressure corrections are necessary as the liquid expands with increasing temperature. Thus, with increasing temperature, the MS-CG pair potentials alone provide an increasingly accurate approximation to the density-dependence of the PMF. Nevertheless, at 175 K a pressure correction of approximately -1.5 kbar is still necessary to accurately model the atomic pressure.

Figure 6(b) presents the temperature-dependence of the pressure-matching coefficients that have been optimized for modeling the constant NPT ensemble at 1 bar external pressure and the indicated temperatures. The solid black circles and solid red squares indicate the optimized values for ψ_1 and ψ_2, respectively. The corresponding lines present fits to these optimized parameters according to Table II. The average pressure correction, ψ_1, varies linearly with temperature. Conversely, the correction for the compressibility, ψ_2, demonstrates less systematic temperature-dependence.

Figure 7 assesses the accuracy of the CG potentials for reproducing the structure and pressure of the AA ethane model at representative state points. The Supporting Information provides a more comprehensive assessment of the CG models.

Figure 7(a) illustrates the accuracy of the CG potentials for modeling the state points from which they were derived. Specifically, Fig. 7(a) presents results from constant NPT simulations at a temperature $T_0 = 150$ K and a fixed external pressure $P_0 = 1$ bar. The solid black curves in Fig. 7(a) present results for the AA model. The dashed red curves present

corresponding results for a CG model with pair potentials and a volume potential derived from these AA simulations. Figure 7(a1) compares the rdfs sampled by the AA and CG simulations. With the exception of a slight discrepancy in the height of the first peak, the CG model reproduces the AA rdf with essentially quantitative accuracy. Figure 7(a2) presents the average pressure sampled by the constant NPT simulations as a function of volume. In this and subsequent figures, we estimate the statistical uncertainty in the pressure by the standard error, as defined in Sec. III A.

From the slope of the simulated average pressures, we determine the compressibility to be $\kappa_T = 9.439 \times 10^{-5}$ bar^{-1} for the AA model. The compressibility and the average volume, $\bar{V}$, determine the standard deviation for the volume fluctuations, $\sigma_V = \sqrt{\bar{V} k_B T \kappa_T} = 0.372$ nm^3, sampled by the AA model at 1 bar external pressure,[90] which indeed agrees well with the distribution of sampled volumes presented in Supporting Fig. S6. When the liquid phase pressure equation of state is extended over this broad range of volumes sampled at 1 bar external pressure, the AA model samples a correspondingly broad range of positive and negative pressures.

More importantly, Fig. 7(a2) demonstrates that the CG model accurately reproduces the average pressure and also the compressibility of the AA model over the range of volumes that are sampled with significant probability. Equivalently, Supporting Fig. S6 demonstrates that the CG model also reproduces the distribution of volumes sampled by the AA model. In particular, the CG model reproduces to within 0.01% and 5.34%, the average and standard deviation, respectively, of the volumes sampled by the AA model at 1 bar external pressure. The SI demonstrates that, more generally, each CG model accurately describes the AA ethane model at the state point from which it had been derived.

Figure 7(b) illustrates the accuracy of CG potentials that have been predicted for modeling new state points. Specifically, Fig. 7(b) presents results from constant NPT simulations of ethane at a temperature T =110 K and a fixed external pressure P_0 =1 bar. The solid black curves in Fig. 7(b) present results for the AA model. The dashed red curves present corresponding results for a CG model with predicted pair and volume potentials. In particular, we predicted the CG pair potential according to Eq. (30) by employing (1) the MS-CG pair potential $U_2(r; T_0, \rho_0)$ calculated from constant NVT simulations at the temperature $T_0 = 150$ K and density $\rho_0 = 618.7$ g/L, (2) the estimate $\partial_T \overline{U}(r)$ for its temperature derivative at constant density, which is presented as the cyan curve in Fig. 3(b), and (3) the

estimate $\partial_\rho \overline{U}(r)$ for its density derivative at constant temperature, which is presented as the cyan curve in Fig. 5(a). Similarly, we predicted the parameters, ψ_1 and ψ_2, for the volume potential according to the lines indicated in Fig. 6 and Table II.

Figure 7(b1) demonstrates that these predicted potentials reproduce the AA rdf quite accurately. The red curve in Fig. 7(b2) indicates that the predicted potentials also provide a reasonable description of the AA pressure-volume equation of state. Specifically, the predicted potentials overestimate the AA density by 0.88%, while underestimating the compressibility by 26%. If a more accurate description of the AA pressure-volume equation of state is needed, the predicted volume potential can be easily refined by one or two iterations of self-consistent pressure-matching. The dashed green curve in Fig. 7(b2) presents the CG pressure-volume equation of state using the predicted pair potentials along with the refined volume potential. The open symbols in Fig. 6(b) indicate the resulting optimized parameters for the volume potentials. The optimized parameters, ψ_1 and ψ_2, differ by 0.19 kJ/mol and 6.7 kJ/mol, respectively, from those predicted by the linear extrapolation. Thus, simple linear extrapolation provides a fairly accurate prediction for ψ_1, but not for ψ_2. The SI demonstrates that the linear extrapolation predicts potentials that provide similar accuracy for modeling ethane in the constant NPT ensemble at $T = 165$ K and 1 bar external pressure.

As a final point of comparison, we consider again constant NVT simulations of AA and CG models at the state point, temperature $T_0 = 150$ K and density $\rho_0 = 618.7$ g/L, that was employed in determining the reference MS-CG pair potential, $U_2(r; T_0, \rho_0)$. The isolated black star in Fig. 7(a2) indicates the volume and average pressure of the AA simulation. The overlapping red triangle in Fig. 7(a2) indicates the volume and average pressure of a CG model employing the pair and volume potentials that had been determined from constant NPT simulations at the same temperature T_0 and 1 bar external pressure. (The green curves in Figs. 4(c) and 6(a) correspond to these pair and volume potentials, while the dashed red curves in Fig. 7(a) present the rdf and pressure equation of state from this constant NPT simulation.) These CG potentials reproduce the average pressure of the AA simulation to within 3.5% error. The SI demonstrates that this CG simulation also accurately reproduces the AA rdf. Conversely, the red asterisk in Fig. 7(a2) presents the average pressure of a CG simulation when the same volume potential is combined with the reference MS-CG pair potential that had been optimized from constant NVT simulations at this state point. (This potential is indicated by the green curve in Fig. 1(c).) Because the reference pair potential is

significantly more repulsive than the pair potential parameterized at atmospheric pressure, the CG model now overestimates the AA pressure by approximately 1500 bar. Thus, pair and volume potentials that have been parameterized for simulating atmospheric pressure conditions at a specified temperature appear to provide an accurate description of the AA pressure over a surprisingly wide density range. However, when combining this volume potential with a very different pair potential, the resulting CG model does not accurately describe the AA pressure.

B. Methanol

Figure 8 characterizes the pair structure and effective interactions generated by atomically detailed simulations of methanol that sample the constant NVT ensemble with a density $\rho_0 = 792.3$ g/L. In Figs. 8-12(a), the black, red, green, blue, and purple curves present results for simulations at $T = 200$ K, 225 K, 250 K, 275 K, and 300 K, respectively.

Figure 8(a) presents the rdfs obtained by mapping the atomistic constant NVT simulations to the 1-site CG representation. While the ethane rdf features a single broad peak spanning the range 0.3 nm $< r <$ 0.625 nm, the same region of the methanol rdf features two distinct peaks. While the second peak corresponds to van der Waals contacts, the more prominent first peak corresponds to hydrogen-bonding interactions that are not present in ethane. This hydrogen-bonding peak drops significantly with increasing temperature, while the minimum between these two peaks simultaneously rises. Otherwise, the remainder of the methanol rdf varies with temperature in a manner that is quite similar to the ethane rdf. In particular, the van der Waals peak very slightly decreases with increasing temperature, while the remainder of the rdf is essentially independent of temperature.

Figure 8(b) presents the corresponding pair pmfs. Interestingly, the hydrogen-bonding minimum demonstrates very little temperature sensitivity, suggesting its energetic origin. In contrast, the remainder of the methanol pair pmf varies with temperature in a manner similar to the ethane pair pmf. In particular, the van der Waals minimum deepens with temperature, while the subsequent extrema slightly grow with temperature.

Figure 8(c) presents the corresponding MS-CG pair potentials. In particular, the potential at $T = 300$ K agrees nicely with 1-site MS-CG pair potentials previously reported for the constant NVT ensemble at this temperature.[69,103] As observed for ethane, these pair

potentials are primarily repulsive. However, in contrast to the ethane MS-CG potentials, the methanol potentials reflect two minima superimposed upon this general repulsion: a narrow local minimum that corresponds to hydrogen-bonding interactions at short distances and a broader, lower energy minimum that corresponds to van der Waals interactions at larger distances. As observed for ethane, the MS-CG pair potentials systematically increase with increasing temperature. In particular, the two minima gradually disappear with increasing temperature.

Figure 8(d) presents the indirect contribution to the methanol pair pmf. Interestingly, w_{ind} is quite similar for ethane and for methanol. In both cases the surrounding environment generates a significant effective attraction that stabilizes the contact minimum of the pmf, although this solvation force is somewhat weaker for methanol than for ethane. Moreover, in both cases this effective attraction grows stronger with increasing temperature.

Figure 9 quantifies the temperature variation in the pair pmf, $\partial_T w_2$, the MS-CG pair potential, $\partial_T U_2$, and the solvation potential, $\partial_T w_{\text{ind}}$, for methanol according to Eq. (28). The potentials appear to vary quite linearly with temperature over the range 225 K $\leq T \leq$ 300 K, although the MS-CG potentials appear to behave somewhat differently closer to the freezing point at $T = 200$ K. Moreover, this temperature variation is generally similar to that quantified in Fig. 3 for ethane. As observed for ethane, $\partial_T w_2$ is relatively small and oscillates around 0, due to the cancellation between $\partial_T U_2$ and $\partial_T w_{\text{ind}}$, which are positive and negative, respectively. Interestingly, $\partial_T w_2$ demonstrates a rather sharp minima at $r \approx$ 0.4 nm that corresponds to the barrier between the hydrogen-bonding and van der Waals contact minima of the methanol pmf. For shorter distances that reflect specific interactions, $\partial_T U_2$ is considerably smaller for methanol than for ethane. In particular, U_2 appears to vary differently with temperature for distances corresponding to hydrogen-bonding and van der Waals interactions with a noticeable transition at $r \approx 0.4$ nm. Lu and Voth have previously reported similar results for the temperature variation of the MS-CG pair potential for methanol at constant density and have interpreted this variation in terms of an entropic pair potential.[38]

Figure 10 presents the rdf, pair pmf, and MS-CG pair potential obtained from atomic simulations of methanol at different temperatures, but the same constant external pressure of 1 bar. Note that the methanol density decreases by 12% over this temperature range, which is slightly smaller than the observed density decrease for ethane. As observed at

constant density, the rdf peaks generally decrease with increasing temperature. Also, as observed for ethane, the constant NPT rdfs and pair pmfs demonstrate a noticeable shift to larger distances with increasing temperature that is not observed at constant density. Presumably due to the specific hydrogen-bonding interactions and the smaller density variation in methanol, this shift is less pronounced for methanol than for ethane. It is interesting that the hydrogen-bonding minimum of the methanol pair pmf slightly decreases with increasing temperature at constant pressure, but not at constant density. It is also interesting that the hydrogen-bonding minimum of the MS-CG potential does not shift to larger distances with increasing temperature in either the constant volume or constant pressure ensemble. Conversely, the barrier between hydrogen-bonding and van der Waals interactions does shift to larger distances as the liquid expands with increasing temperature at constant pressure. Most striking, though, is that the MS-CG potentials again become increasingly attractive with increasing temperature at constant pressure. This is opposite to the trend observed for methanol at constant density, but is consistent with the preceding observations for ethane at constant pressure.

Figure 11(a) presents the finite difference estimate, $\partial_\rho U$, for the density derivative of the MS-CG potentials, $(\partial U/\partial\rho)_{r,T}$, in analogy to Fig. 5(a). As in Fig. 5(a), the noticeable variation for $r < 0.27$ nm reflects poor statistics and numerical extrapolation into the hard-core region of the potential. As observed for ethane, the methanol MS-CG potentials systematically increase with density at constant temperature. This density derivative is largest at small distances and systematically decreases with increasing distance. With the exception of the results for 200 K, this density dependence appears even more linear for methanol than for ethane. Interestingly, the deviations from linearity are most pronounced at short hydrogen-bonding distances. It is also interesting that, presumably due to the formation of specific short-ranged hydrogen bonds, the MS-CG potentials demonstrate considerably less density-dependence for methanol than for ethane. Furthermore, the density derivatives for methanol demonstrate an inflection point that corresponds to the barrier between hydrogen-bonding and van der Waals contacts. Figure 11(b) compares the MS-CG pair potentials calculated from constant pressure simulations at each temperature with potentials predicted by a linear extrapolation of a single pair potential obtained at constant density, i.e., according to Eq. (30). This extrapolation appears even more accurate for methanol than for ethane, although the potential at $T = 200$ K is slightly underestimated.

Figure 12 presents the pressure corrections, F_V, that have been optimized for simulating methanol at 1 bar external pressure and the specified temperatures. As observed for ethane, the magnitude of the pressure correction systematically decreases with increasing temperature. Moreover, ψ_1, which quantifies the mean pressure correction, again varies linearly with temperature. Interestingly, ψ_1 varies less rapidly with temperature for methanol than for ethane. Consequently, near their freezing points ethane requires a larger pressure correction, but near their boiling points methanol requires a larger pressure correction. As observed for ethane, Fig. 12 also demonstrates that the calculated ψ_2 parameters do not vary linearly with temperature. More importantly, though, the SI demonstrates that volume potentials predicted by this simple linear extrapolation describe methanol density fluctuations with reasonable, though not quantitative, accuracy.

Finally, Fig. 13 demonstrates the accuracy of the calculated and predicted CG potentials for methanol in analogy to Fig. 7. The top and bottom rows present results from constant NPT simulations of AA (solid black curves) and CG (dashed red curves) models at 1 bar external pressure and temperatures $T = 250$ K and 210 K, respectively.

Figure 13(a) assesses the accuracy of CG potentials that were explicitly calculated for modeling the specified state point. The CG potentials accurately reproduce not only the AA pair structure, but also the AA average pressure as a function of volume over the sampled volume range. In particular, the CG model reproduces the density and compressibility of the AA model to within 0.05% and 3.93%, respectively. The SI demonstrates that, more generally, each CG model accurately describes the AA methanol model at the state point for which it had been derived.

Fig. 13(b) then assesses the accuracy of CG potentials that were predicted via linear extrapolation. Fig. 13(b) demonstrates that the predicted potentials accurately reproduce the AA pair structure and also provide a reasonable approximation for the AA pressure equation of state. The predicted CG potentials reproduce the density and compressibility of the AA model to within errors of 1.9% and 8.7%, respectively. The green curve presents results after further refining the predicted volume potential. The optimized values for ψ_1 and ψ_2, which are indicated by the open symbols in Fig. 12(b), differ by 1.2 kJ/mol and 4.2 kJ/mol from the values estimated from linear extrapolation. The SI demonstrates that the linear extrapolation predicts potentials that provide similar accuracy for modeling methanol in the constant NPT ensemble at $T = 290$ K and 1 bar external pressure.

As a final point of comparison, we consider again constant NVT simulations of AA and CG models at the state point, temperature $T_0 = 250$ K and density $\rho_0 = 792.3$ g/L, that was employed in determining the reference MS-CG pair potential, $U_2(r; T_0, \rho_0)$. The isolated black star in Fig. 13(a2) indicates the volume and average pressure of the AA simulation. The overlapping red triangle in Fig. 13(a2) indicates the volume and average pressure of a CG model employing the pair and volume potentials that had been determined from constant NPT simulations at the same temperature T_0 and 1 bar external pressure. (The green curves in Figs. 10(c) and 12(a) correspond to these pair and volume potentials, while the dashed red curves in Fig. 13(a) present the rdf and pressure equation of state from this constant NPT simulation.) These CG potentials reproduce the average pressure of the AA simulation to within 4.8% error, although the SI demonstrates that they provide a somewhat less accurate description of the AA rdf. Conversely, the red asterisk in Fig. 13(a2) presents the average pressure of a CG simulation when the same volume potential is combined with the reference MS-CG pair potential that had been optimized from constant NVT simulations at this state point. (This potential is indicated by the green curve in Fig. 8(c).) In this case, the CG model now underestimates the AA pressure by approximately 1500 bar. Thus, as noted for ethane, pair and volume potentials that have been parameterized for simulating atmospheric pressure conditions at a specified temperature appear to provide an accurate description of the AA pressure over a surprisingly wide density range. However, when combining this volume potential with a very different pair potential, the resulting CG model provides a poor description of the AA pressure.

V. DISCUSSION

In this work we have carefully examined the state-point dependence of effective pair potentials calculated for 1-site MS-CG models of liquid ethane and methanol. The methanol pair potential includes a metastable minimum at short distances corresponding to hydrogen-bonding configurations. Otherwise, the calculated MS-CG pair potentials are quite similar for these two molecules, being primarily repulsive, quite short-ranged, and essentially vanishing for $r > 0.65$ nm. Consequently, the CG models for both molecules require rather large pressure corrections in order to stabilize the liquid phase at 1 bar external pressure.

The calculated MS-CG pair potentials vary quite linearly over a fairly wide temperature

range at constant density. Moreover, the corresponding temperature derivatives, $\partial_T U$, are qualitatively similar for ethane and methanol. These temperature derivatives are almost everywhere positive, reach a maximum at contact, decrease with increasing distance, and become negligible for $r > 0.65$ nm. For $r < 0.5$ nm, the temperature derivative is significantly smaller for methanol for ethane, which is presumably due to the specific hydrogen-bonding interactions that form at short distances.

Although we did not emphasize this, Figs. 7 and 13, as well as the SI, demonstrate that the CG models accurately describe the pair structure and pressure-volume equation of state at each state point considered. Consequently, the MS-CG potentials $U = U_R + U_V$ appear to quite accurately approximate the configuration-, temperature-, and volume-dependence of the many-body PMF, W_N. In particular, Eq. (12) indicates that W_N increases with temperature in every configuration, while our calculations indicate that the MS-CG interaction potential, U_R, also increases with temperature in every configuration. It is encouraging that the MS-CG variational principle appears sufficiently sensitive to the configuration-dependence of the many-body PMF that it at least qualitatively reproduces the variation of W_N with temperature.

Conversely, the pair pmf does not increase at all distances with increasing temperature at constant density. In fact in the case of ethane, which lacks significant specific attractions, the contact minimum of the pair pmf becomes increasingly attractive with increasing temperature. This increasing attraction does not reflect the direct interaction between pairs of molecules. As noted above, the MS-CG pair potential, which quantifies this direct interaction, becomes increasingly repulsive with increasing temperature. Instead the increasing depth of the contact minimum in the ethane pair pmf reflects increasing repulsion from the surrounding molecules. In this case it is quite interesting that the MS-CG potential and the many-body PMF both become increasingly repulsive with temperature, although the pair and three-body correlations appear quite insensitive to temperature.

We also find that the MS-CG pair potentials for ethane and methanol both become increasingly repulsive with increasing density at constant temperature. Interestingly, the density derivatives at constant temperature appear qualitatively similar to the temperature derivatives at constant density. The density derivatives are largest at contact and systematically decrease with increasing distance, vanishing for $r > 0.65$ nm. As noted above for the temperature derivatives, at short distances corresponding to hydrogen-bonding interactions

the density derivative is considerably smaller for methanol than for ethane.

This density-dependence leads to the striking result that the MS-CG pair potentials become increasingly *attractive* with increasing temperature at constant external pressure. Indeed, similar trends have been previously observed for 1-site CG models of liquid water that were optimized to match AA rdfs.[16,37] This suggests that the density-dependence may, in some cases, be more important than the temperature-dependence of effective potentials for CG models of liquids near ambient conditions. It is beyond the scope of this work to definitively determine the physical origin for this surprising observation. Nevertheless, it is intriguing to speculate that this may be a general feature of pair potentials that reflect distinct molecular interactions acting on different length scales. In this case, the dramatic changes in the effective pair potentials may result from reweighting the contributions of these interactions.

Additionally, we observe that the volume force necessary for simulating atmospheric pressure systematically decreases with increasing temperature. This is consistent with the observation that the MS-CG pair potentials become less repulsive as the liquid expands with increasing temperature at constant external pressure. In particular, we find that the mean pressure correction at 1 bar pressure, which is specified by ψ_1, varies linearly with temperature. Interestingly, ψ_1 varies more rapidly with temperature for ethane than for methanol.

These results are quite consistent with the very recent study of Rosenberger and van der Vegt,[104] who parameterized pair potentials for CG models of hexane and perfluorohexane at a single state point with the structure-based inverse Monte Carlo (IMC) method.[74] They then employed self-consistent pressure-matching[82,98] to determine the coefficients, ψ_1 and ψ_2, that were necessary for simulating a range of temperatures at 1 bar external pressure. They observed that both ψ_1 and ψ_2 linearly decreased with temperature. In contrast, in our calculations ψ_2, which specifies the correction to the compressibility, does not vary linearly with temperature. This discrepancy most likely results from their use of a single set of pair potentials, while we considered separate pair potentials for each state point. However, this discrepancy may also possibly reflect differences between the MS-CG and IMC potentials or differences between the systems considered.

Finally, our studies also have significant pragmatic consequences. Importantly, in this work we extrapolated potentials obtained from the NVT ensemble to predict potentials for

use in the constant NPT ensemble. Thus, effective potentials can be transferred between ensembles as long as they appropriately account for the relevant thermodynamic contributions. In particular, consistency between the NVT and NPT ensembles requires that the CG potentials account for the volume-dependence of the many-body PMF. This can be easily achieved in practice by accurately determining the volume potential, U_V.

Additionally, while some prior studies have proposed more complex temperature dependence,[41,42] our calculations indicate that the effective pair potentials and mean pressure corrections for 1-site CG models of ethane and methanol vary quite linearly with temperature and density over a fairly wide range of thermodynamic conditions, as noted by several prior studies.[38–40] We observe slight deviations from linearity that may reflect either higher order derivatives of the PMF or statistical uncertainty in our calculations. Nevertheless, a simple linear extrapolation quite accurately predicts both the MS-CG pair potential and the average pressure correction, though not the compressibility correction, for both liquids across a fairly wide range of temperatures at atmospheric pressure. In particular, Figs. 7 and 13, as well as the SI, demonstrate that this extrapolation predicts potentials that quite reasonably describe the pair structure, pressure-volume behavior, and density fluctuations of the atomistic model for state points that were not employed in developing this extrapolation.

We also demonstrated that pair and volume potentials that have been self-consistently optimized provide a remarkably accurate description of the AA internal pressure over a surprisingly broad density range in either the constant NVT or constant NPT ensemble. In particular, potentials that have been parameterized for modeling atmospheric pressure and a specified temperature quite accurately approximated AA pressures of +470 bar and -502 bar that were calculated from constant NVT simulations of ethane and methanol, respectively. As described above, when both pair and volume potentials are predicted via linear extrapolation, the resulting CG models provide a reasonably accurate description of the AA pressure equation of state for state points near atmospheric pressure. However, when both pair and volume potentials are predicted for state points far from atmospheric pressure, this simple linear extrapolation provides a poor description of the AA pressure. In such cases, the predicted volume potential may need to account for the density-dependence of the predicted pair potentials.

We emphasize that we do not anticipate that effective potentials will always vary linearly with variations in thermodynamic state point. More generally, we expect that the state-point

dependence of approximate effective potentials will reflect (1) the state-point dependence of the many-body PMF and (2) the accuracy with which the effective potentials approximate the PMF. Equation 12 indicates that $(\partial W_N/\partial T)_{\mathbf{R},V} = -S_W$, which quantifies the "internal" entropy associated with the conditioned distribution, $p_{r|R}$, of atomic configurations, $\mathbf{r}$, that map to $\mathbf{R}$.

If over a specified temperature range, this conditioned distribution varies little, then S_W will be approximately constant and W_N will vary approximately linearly with temperature. Because ethane and methanol demonstrate little intramolecular flexibility, one expects that S_W for the 1-site representation will be relatively small in magnitude and demonstrate relatively little temperature-dependence within the liquid region of the phase diagram. Moreover, the MS-CG potentials accurately approximate the configuration- and volume-dependence of the PMF. Thus, one expects that the MS-CG potentials will vary quite linearly with temperature. Our calculations provide numerical support for this intuitive expectation.

Conversely, for molecules with greater internal flexibility and in cases that the CG mapping imposes relatively weaker constraints upon the atomic configuration, one expects that S_W will be larger and more sensitive to temperature. In particular, if the CG representation maps multiple distinct conformations to the same CG configuration, i.e., if the CG configuration is consistent with multiple "internal states,"[105,106] then one expects that S_W will vary rapidly with temperature when the atomic degrees of freedom "switch" between internal states. In such cases, one expects that both W_N and also approximate effective potentials will vary more dramatically with temperature. Future work is certainly required to further investigate these more complex situations. Nevertheless, recent work provides encouraging hints that considerable transferability can be achieved even for very aggressive coarse-graining of highly charged ionomers.[46]

In closing, we note several additional directions for future work. In this work we considered the temperature and density dependence of CG potentials for modeling ethane and methanol in the liquid phase, while primarily focusing upon conditions at or near atmospheric pressure. Further study is necessary to assess the generality of the trends observed in this work for modeling the entire liquid phase diagram, as well as for modeling other chemical systems.[33,107,108] Moreover, future work should investigate the importance of this state-point dependence for modeling phase transitions and dynamical processes. It remains

very challenging to reproduce phase transitions with bottom-up CG models,[25,30] although recent studies have suggested that potentials of the local density may prove useful for modeling two-phase coexistence.[66–68] One generally anticipates that effective potentials will vary dramatically across phase boundaries due to significant changes in the conditioned distribution, $p_{r|R}$, of atomic configurations for a given CG configuration. For similar reasons, one intuitively expects that the state point dependence of effective potentials should also complicate the dynamics of CG models. For instance, changes in $p_{r|R}$ may alter the "internal energy" of CG sites in dissipative particle dynamics (DPD) models with energy conservation,[109,110] as well the properties of "fictitious particles" that mimic the random forces due to atoms that have been eliminated from the CG model.[111,112] Thus, considerable work remains for understanding the fundamental and practical aspects of the state-point dependence of effective potentials employed in CG models.

SUPPLEMENTARY MATERIAL

The Supplementary Material presents comparisons of AA and CG rdfs, volume distributions, and pressure-volume equations of state that assess the accuracy of the potentials presented in the main text, as well as the predictive power of the proposed linear extrapolations.

ACKNOWLEDGEMENTS

The authors gratefully acknowledge financial support from the National Science Foundation (Grant No. CHE-1565631). K. M. Lebold was supported by a fellowship from The Molecular Sciences Software Institute under NSF grant ACI-1547580. The authors also thank Varun Mandalaparthy and Michael Delyser for their assistance in analyzing our calculations. Portions of this research were conducted with Advanced CyberInfrastructure computational resources provided by The Institute for CyberScience at The Pennsylvania State University (http://ics.psu.edu). In addition, parts of this research were conducted with XSEDE resources awarded by TG-CHE150090 and TG-CHE170062.

REFERENCES

[1]C. N. Likos, "Effective interactions in soft condensed matter physics," Phys. Rep. **348**, 267 – 439 (2001).

[2]M. L. Klein and W. Shinoda, "Large-scale molecular dynamics simulations of self-assembling systems," Science **321**, 798–800 (2008).

[3]T. Murtola, A. Bunker, I. Vattulainen, M. Deserno, and M. Karttunen, "Multiscale modeling of emergent materials: Biological and soft matter," Phys. Chem. Chem. Phys. **11**, 1869–92 (2009).

[4]S. Riniker, J. R. Allison, and W. F. van Gunsteren, "On developing coarse-grained models for biomolecular simulation: a review," Phys. Chem. Chem. Phys. **14**, 12423–12430 (2012).

[5]W. G. Noid, "Perspective: coarse-grained models for biomolecular systems," J. Chem. Phys. **139**, 090901 (2013).

[6]E. Brini, E. A. Algaer, P. Ganguly, C. Li, F. Rodríguez-Ropero, and N. F. A. van der Vegt, "Systematic coarse-graining methods for soft matter simulations - a review," Soft Matter **9**, 2108–2119 (2013).

[7]M. G. Saunders and G. A. Voth, "Coarse-graining methods for computational biology," Annu. Rev. Biophys. **42**, 73–93 (2013).

[8]R. L. C. Akkermans and W. J. Briels, "A structure-based coarse-grained model for polymer melts," J. Chem. Phys. **114**, 1020–1031 (2001).

[9]F. H. Stillinger, H. Sakai, and S. Torquato, "Statistical mechanical models with effective potentials: Definitions, applications, and thermodynamic consequences," J. Chem. Phys. **117**, 288–296 (2002).

[10]H. Wang, C. Junghans, and K. Kremer, "Comparative atomistic and coarse-grained study of water: What do we lose by coarse-graining?" Eur. Phys. J. E: Soft Matter Biol. Phys. **28**, 221–229 (2009).

[11]G. D'Adamo, A. Pelissetto, and C. Pierleoni, "Predicting the thermodynamics by using state-dependent interactions," J. Chem. Phys. **138**, 234107 (2013).

[12]M. Guenza, "Thermodynamic consistency and other challenges in coarse-graining models," Eur. Phys. J.: Spec. Top. **224**, 2177–2191 (2015).

[13]J. W. Wagner, J. F. Dama, A. E. P. Durumeric, and G. A. Voth, "On the representability problem and the physical meaning of coarse-grained models," J. Chem. Phys. **145**, 044108 (2016).

[14]N. J. H. Dunn, T. T. Foley, and W. G. Noid, "Van der waals perspective on coarse-graining: progress toward solving representability and transferability problems," Acc. Chem. Res. **49**, 2832–2840 (2016).

[15]A. A. Louis, "Beware of density dependent pair potentials," J. Phys.: Condens. Matter **14**, 9187–9206 (2002).

[16]M. E. Johnson, T. Head-Gordon, and A. A. Louis, "Representability problems for coarse-grained water potentials," J. Chem. Phys. **126**, 144509 (2007).

[17]J. G. Kirkwood, "Statistical mechanics of fluid mixtures," J. Chem. Phys. **3**, 300–313 (1935).

[18]A. Liwo, S. Ołdziej, M. R. Pincus, R. J. Wawak, S. Rackovsky, and H. A. Scheraga, "A united-residue force field for off-lattice protein-structure simulations. i. Functional forms and parameters of long-range side-chain interaction potentials from protein crystal data," J. Comp. Chem. **18**, 849–873 (1997).

[19]W. G. Noid, "Systematic methods for structurally consistent coarse-grained models," Methods Mol Biol **924**, 487–531 (2013).

[20]A. J. Clark, J. McCarty, I. Y. Lyubimov, and M. G. Guenza, "Thermodynamic consistency in variable-level coarse graining of polymeric liquids," Phys. Rev. Lett. **109**, 168301 (2012).

[21]J. McCarty, A. J. Clark, I. Y. Lyubimov, and M. G. Guenza, "Thermodynamic consistency between analytic integral equation theory and coarse-grained molecular dynamics simulations of homopolymer melts," Macromolecules **45**, 8482–8493 (2012).

[22]J. McCarty, A. J. Clark, J. Copperman, and M. G. Guenza, "An analytical coarse-graining method which preserves the free energy, structural correlations, and thermodynamic state of polymer melts from the atomistic to the mesoscale," J. Chem. Phys. **140**, 204913 (2014).

[23]M. Dinpajooh and M. G. Guenza, "Thermodynamic consistency in the structure-based integral equation coarse-grained method," Polymer **117**, 282–286 (2017).

[24]T. T. Foley, M. S. Shell, and W. G. Noid, "The impact of resolution upon entropy and information in coarse-grained models," J. Chem. Phys. **143**, 243104 (2015).

[25]J. Ghosh and R. Faller, "State point dependence of systematically coarse-grained potentials," Mol. Simul. **33**, 759–767 (2007).

[26]P. Carbone, H. A. K. Varzaneh, X. Chen, and F. Müller-Plathe, "Transferability of coarse-grained force fields: The polymer case," J. Chem. Phys. **128**, 064904 (2008).

[27]Y. T. Wang, W. G. Noid, P. Liu, and G. A. Voth, "Effective force coarse-graining," Phys. Chem. Chem. Phys. **11**, 2002–2015 (2009).

[28]D. M. Huang, R. Faller, K. Do, and A. J. Moule, "Coarse-grained computer simulations of polymer/fullerene bulk heterojunctions for organic photovoltaic applications," J. Chem. Theory Comput. **6**, 526–537 (2010), pMID: 26617308, https://doi.org/10.1021/ct900496t.

[29]G. Megariotis, A. Vyrkou, A. Leygue, and D. N. Theodorou, "Systematic coarse graining of 4-cyano-4′-pentylbiphenyl," Ind. Eng. Chem. Res. **50**, 546–56 (2011).

[30]B. Mukherjee, L. Delle Site, K. Kremer, and C. Peter, "Derivation of coarse grained models for multiscale simulation of liquid crystalline phase transitions," J. Phys. Chem. B **116**, 8474–8484 (2012).

[31]J. Zhang and H. Guo, "Transferability of coarse-grained force field for ncb liquid crystal systems," J. Phys. Chem. B **118**, 4647–4660 (2014).

[32]Q. Xiao and H. Guo, "Transferability of a coarse-grained atactic polystyrene model: the non-bonded potential effect," Phys. Chem. Chem. Phys. **18**, 29808–29824 (2016).

[33]J. W. Mullinax and W. G. Noid, "Extended ensemble approach for deriving transferable coarse-grained potentials," J. Chem. Phys. **131**, 104110 (2009).

[34]T. C. Moore, C. R. Iacovella, and C. McCabe, "Derivation of coarse-grained potentials via multistate iterative boltzmann inversion," J. Chem. Phys. **140**, 224104 (2014).

[35]T. Vettorel and H. Meyer, "Coarse graining of short polyethylene chains for studying polymer crystallization," J. Chem. Theory Comput. **2**, 616–629 (2006).

[36]Y. T. Wang, S. Izvekov, T. Y. Yan, and G. A. Voth, "Multiscale coarse-graining of ionic liquids," J. Phys. Chem. B **110**, 3564 – 3575 (2006).

[37]A. Chaimovich and M. S. Shell, "Anomalous waterlike behavior in spherically-symmetric water models optimized with the relative entropy," Phys. Chem. Chem. Phys. **11**, 1901–1915 (2009).

[38]L. Lu and G. A. Voth, "The multiscale coarse-graining method. VII. Free energy decomposition of coarse-grained effective potentials," J. Chem. Phys. **134**, 224107 (2011).

[39]S. Izvekov, "Towards an understanding of many-particle effects in hydrophobic association in methane solutions," J. Chem. Phys. **134**, 034104 (2011).

[40]K. Farah, A. C. Fogarty, M. C. Böhm, and F. Müller-Plathe, "Temperature dependence of coarse-grained potentials for liquid hexane," Phys. Chem. Chem. Phys. **13**, 2894–902 (2011).

[41]A. Liwo, M. Khalili, C. Czaplewski, S. Kalinowski, S. Ołdziej, K. Wachucik, and H. A. Scheraga, "Modification and optimization of the united-residue (UNRES) potential energy function for canonical simulations. I. Temperature dependence of the effective energy function and tests of the optimization method with single training proteins," J. Phys. Chem. B **111**, 260–85 (2007).

[42]H.-J. Qian, P. Carbone, X. Chen, H. A. Karimi-Varzaneh, C. C. Liew, and F. Müller-Plathe, "Temperature-transferable coarse-grained potentials for ethylbenzene, polystyrene and their mixtures," Macromolecules **41**, 9919–29 (2008).

[43]V. Krishna, W. G. Noid, and G. A. Voth, "The multiscale coarse-graining method. iv. transferring coarse-grained potentials between temperatures," J. Chem. Phys. **131**, 024103 (2009).

[44]A. Mirzoev and A. P. Lyubartsev, "Effective solvent mediated potentials of na^+ and cl^- ions in aqueous solution: temperature dependence," Phys. Chem. Chem. Phys. **13**, 5722–5727 (2011).

[45]Z. Cao, J. F. Dama, L. Lu, and G. A. Voth, "Solvent free ionic solution models from multiscale coarse-graining," J. Chem. Theory Comput. **9**, 172–178 (2013).

[46]J. F. Rudzinski, K. Lu, S. T. Milner, J. K. Maranas, and W. G. Noid, "Extended ensemble approach to transferable potentials for low-resolution coarse-grained models of ionomers," J. Chem. Theory Comput. **13**, 2185–2201 (2017).

[47]F. Cao and H. Sun, "Transferability and nonbond functional form of coarse grained force field – tested on linear alkanes," J. Chem. Theory Comput. **11**, 4760–4769 (2015).

[48]D. D. Hsu, W. Xia, S. G. Arturo, and S. Keten, "Thermomechanically consistent and temperature transferable coarse-graining of atactic polystyrene," Macromolecules **48**, 3057–3068 (2015).

[49]W. Xia, J. Song, C. Jeong, D. D. Hsu, J. Phelan, Frederick R., J. F. Douglas, and S. Keten, "Energy-renormalization for achieving temperature transferable coarse-graining of polymer dynamics," Macromolecules **50**, 8787–8796 (2017).

[50]A. Tsourtis, V. Harmandaris, and D. Tsagkarogiannis, "Parameterization of Coarse-Grained Molecular Interactions through Potential of Mean Force Calculations and Cluster Expansion Techniques," Entropy **19**, 395 (2017).

[51]M. Dinpajooh and M. G. Guenza, "On the Density Dependence of the Integral Equation Coarse-Graining Effective Potential," J. Phys. Chem. B **122**, 3426–3440 (2018).

[52]M. Dijkstra, R. van Roij, and R. Evans, "Direct simulation of the phase behavior of binary hard-sphere mixtures: Test of the depletion potential description," Phys. Rev. Lett. **82**, 117–120 (1999).

[53]A. A. Louis, P. G. Bolhuis, J. P. Hansen, and E. J. Meijer, "Can polymer coils be modeled as "soft colloids"?" Phys. Rev. Lett. **85**, 2522–2525 (2000).

[54]J. Silbermann, S. H. L. Klapp, M. Shoen, N. Channamsetty, H. Block, and K. E. Gubbins, "Mesoscale modeling of complex binary fluid mixtures: Towards an atomistic foundation of effective potentials," J. Chem. Phys. **124**, 074105 (2006).

[55]J. Fischer, D. Paschek, A. Gieger, and G. Sadowski, "Modeling of aqueous poly(oxyethylene) solutions. 2. Mesoscale simulations," J. Phys. Chem. B **112**, 13561–71 (2008).

[56]M. Montes-Saralegui, G. Kahl, and A. Nikoubashman, "On the applicability of density dependent effective interactions in cluster-forming systems," J. Chem. Phys. **146**, 054904 (2017).

[57]B. Hess and N. F. A. van der Vegt, "Hydration thermodynamic properties of amino acid analogues: A systematic comparison of biomolecular force fields and water models," J. Phys. Chem. B **110**, 17616–17626 (2006).

[58]A. Savelyev and G. A. Papoian, "Molecular renormalization group coarse-graining of electrolyte solutions: Applications to aqueous NaCl and KCl," J. Phys. Chem. B **113**, 7785–93 (2009).

[59]J.-W. Shen, C. Li, N. F. van der Vegt, and C. Peter, "Transferability of coarse grained potentials: Implicit solvent models for hydrated ions," J. Chem. Theory Comput. **7**, 1916–1927 (2011).

[60]E. C. Allen and G. C. Rutledge, "A novel algorithm for creating coarse-grained, density dependent implicit solvent models," J. Chem. Phys. **128**, 154115 (2008).

[61]E. C. Allen and G. C. Rutledge, "Evaluating the transferability of coarse-grained, density-dependent implicit solvent models to mixtures and chains," J. Chem. Phys. **130**, 034904

(2009).

[62]S. Izvekov, P. W. Chung, and B. M. Rice, "The multiscale coarse-graining method: Assessing its accuracy and introducing density dependent coarse-grain potentials," J. Chem. Phys. **133**, 064109 (2010).

[63]S. Izvekov, P. W. Chung, and B. M. Rice, "Particle-based multiscale coarse graining with density-dependent potentials: Application to molecular crystals (hexahydro-1,3,5-trinitro-s-triazine)," J. Chem. Phys. **135**, 044112 (2011).

[64]T. Sanyal and M. S. Shell, "Coarse-grained models using local-density potentials optimized with the relative entropy: Application to implicit solvation," J. Chem. Phys. **145**, 034109 (2016).

[65]J. W. Wagner, T. Dannenhoffer-Lafage, J. Jin, and G. A. Voth, "Extending the range and physical accuracy of coarse-grained models: Order parameter dependent interactions," J. Chem. Phys. **147**, 044113 (2017), http://dx.doi.org/10.1063/1.4995946.

[66]M. R. DeLyser and W. G. Noid, "Extending pressure-matching to inhomogeneous systems via local-density potentials," J. Chem. Phys. **147**, 134111 (2017).

[67]T. Sanyal and M. S. Shell, "Transferable coarse-grained models of liquid - liquid equilibrium using local density potentials optimized with the relative entropy," J. Phys. Chem. B **122**, 5678–5693 (2018), pMID: 29466859, https://doi.org/10.1021/acs.jpcb.7b12446.

[68]J. Jin and G. A. Voth, "Ultra-coarse-grained models allow for an accurate and transferable treatment of interfacial systems," J. Chem. Theory Comput. **14**, 2180–2197 (2018), pMID: 29481754, https://doi.org/10.1021/acs.jctc.7b01173.

[69]S. Izvekov and G. A. Voth, "A multiscale coarse-graining method for biomolecular systems," J. Phys. Chem. B **109**, 2469 – 2473 (2005).

[70]S. Izvekov and G. A. Voth, "Multiscale coarse graining of liquid-state systems," J. Chem. Phys. **123**, 134105 (2005).

[71]W. G. Noid, J.-W. Chu, G. S. Ayton, and G. A. Voth, "Multiscale coarse-graining and structural correlations: Connections to liquid state theory," J. Phys. Chem. B **111**, 4116–4127 (2007).

[72]W. G. Noid, J.-W. Chu, G. S. Ayton, V. Krishna, S. Izvekov, G. A. Voth, A. Das, and H. C. Andersen, "The multiscale coarse-graining method. I. A rigorous bridge between atomistic and coarse-grained models," J. Chem. Phys. **128**, 244114 (2008).

[73]F. Müller-Plathe, "Coarse-graining in polymer simulation: From the atomistic to the mesoscopic scale and back," ChemPhysChem **3**, 755 – 769 (2002).

[74]A. P. Lyubartsev and A. Laaksonen, "Calculation of effective interaction potentials from radial distribution functions: a reverse Monte Carlo approach," Phys. Rev. E Stat. Phys. Plasmas Fluids Relat. Interdiscip. Topics **52**, 3730–3737 (1995).

[75]S. Jain, S. Garde, and S. K. Kumar, "Do inverse monte carlo algorithms yield thermodynamically consistent interaction potentials?" Ind. Eng. Chem. Res. **45**, 5614–5618 (2006), http://pubs.acs.org/doi/pdf/10.1021/ie060042h.

[76]J. F. Rudzinski and W. G. Noid, "Bottom-up coarse-graining of peptide ensembles and helix-coil transitions," J. Chem. Theory Comput. **11**, 1278–1291 (2015).

[77]J. F. Rudzinski and W. G. Noid, "A generalized-yvon-born-green method for coarse-grained modeling," Eur. Phys. J.: Spec. Top. **224**, 2193–2216 (2015).

[78]J. W. Mullinax and W. G. Noid, "A generalized Yvon-Born-Green theory for molecular systems," Phys. Rev. Lett. **103**, 198104 (2009).

[79]J. W. Mullinax and W. G. Noid, "A generalized Yvon-Born-Green theory for determining coarse-grained interaction potentials," J. Phys. Chem. C **114**, 5661–5674 (2010).

[80]J. F. Rudzinski and W. G. Noid, "The role of many-body correlations in determining potentials for coarse-grained models of equilibrium structure," J. Phys. Chem. B **116**, 8621–8635 (2012).

[81]A. Das and H. C. Andersen, "The multiscale coarse-graining method. V. Isothermal-isobaric ensemble," J. Chem. Phys. **132**, 164106 (2010).

[82]N. J. H. Dunn and W. G. Noid, "Bottom-up coarse-grained models that accurately describe the structure, pressure, and compressibility of molecular liquids," J. Chem. Phys. **143**, 243148 (2015).

[83]N. J. H. Dunn and W. G. Noid, "Bottom-up coarse-grained models with predictive accuracy and transferability for both structural and thermodynamic properties of heptane-toluene mixtures," J. Chem. Phys. **144**, 204124 (2016).

[84]M. E. Tuckerman., Statistical Mechanics: Theory and Molecular Simulation (Oxford University Press, Oxford, Great Britain, 2013).

[85]A. J. Chorin, "Conditional expectations and renormalization," Multiscale Model. Simul. **1**, 105–118 (2003).

[86]A. J. Chorin, O. H. Hald, and R. Kupferman, "Optimal prediction and the Mori-Zwanzig representation of irreversible processes," Proc. Natl. Acad. Sci. U.S.A. **97**, 2968–73 (2000).

[87]M. S. Shell, "The relative entropy is fundamental to multiscale and inverse thermodynamic problems," J. Chem. Phys. **129**, 144108 (2008).

[88]M. S. Shell, "Coarse-graining with the relative entropy," in Adv. Chem. Phys. (John Wiley & Sons, Inc., 2016) pp. 395–441.

[89]J. W. Mullinax and W. G. Noid, "Reference state for the generalized Yvon-Born-Green theory: Application for a coarse-grained model of hydrophobic hydration," J. Chem. Phys. **133**, 124107 (2010).

[90]T. L. Hill, An Introduction to Statistical Thermodynamics (Addison Wesley Publishing Company, 1987).

[91]S. Pronk, S. Pall, R. Schulz, P. Larsson, P. Bjelkmar, R. Apostolov, M. R. Shirts, J. C. Smith, P. M. Kasson, D. van der Spoel, B. Hess, and E. Lindahl, "Gromacs 4.5: a high-throughput and highly parallel open source molecular simulation toolkit," Bioinformatics **29**, 845–854 (2013), http://bioinformatics.oxfordjournals.org/content/29/7/845.full.pdf+html.

[92]W. L. Jorgensen, D. S. Maxwell, and J. Tirado-Rives, "Development and testing of the OPLS All-Atom force field on conformational energetics and properties of organic liquids," J. Am. Chem. Soc. **118**, 11225–11236 (1996).

[93]T. Darden, D. York, and L. Pedersen, "Particle mesh ewald: An $N \log(N)$ method for ewald sums in large systems," J. Chem. Phys. **98**, 10089–10092 (1993).

[94]W. F. V. Gunsteren and H. J. C. Berendsen, "A leap-frog algorithm for stochastic dynamics," Mol. Simul. **1**, 173–185 (1988), https://doi.org/10.1080/08927028808080941.

[95]M. Parrinello and A. Rahman, "Crystal structure and pair potentials: A molecular-dynamics study," Phys. Rev. Lett. **45**, 1196–1199 (1980).

[96]P. A. Golubkov and P. Ren, "Generalized coarse-grained model based on point multipole and gay-berne potentials," J. Chem. Phys. **125**, 064103 (2006), https://doi.org/10.1063/1.2244553.

[97]P. A. Golubkov, J. C. Wu, and P. Ren, "A transferable coarse-grained model for hydrogen-bonding liquids," Phys. Chem. Chem. Phys. **10**, 2050–7 (2008).

[98]N. J. H. Dunn, K. M. Lebold, M. R. DeLyser, J. F. Rudzinski, and W. Noid, "Bocs: Bottom-up open-source coarse-graining software," J. Phys. Chem. B **122**, 3363–3377

(2018), pMID: 29227668, https://doi.org/10.1021/acs.jpcb.7b09993.

[99]S. Plimpton, "Fast parallel algorithms for short-range molecular dynamics," J. Comp. Phys. **117**, 1 – 19 (1995).

[100]G. J. Martyna, D. J. Tobias, and M. L. Klein, "Constant pressure molecular dynamics algorithms," J. Chem. Phys. **101**, 4177–4189 (1994).

[101]G. J. Martyna, M. E. Tuckerman, D. J. Tobias, and M. L. Klein, "Explicit reversible integrators for extended systems dynamics," Mol. Phys. **87**, 1117–1157 (1996).

[102]G. J. Martyna, M. L. Klein, and M. Tuckerman, "Nosé–hoover chains: The canonical ensemble via continuous dynamics," J. Chem. Phys. **97**, 2635–2643 (1992).

[103]V. Rühle, C. Junghans, A. Lukyanov, K. Kremer, and D. Andrienko, "Versatile object-oriented toolkit for coarse-graining applications," J. Chem. Theory Comput. **5**, 3211–3223 (2009).

[104]D. Rosenberger and N. F. A. van der Vegt, "Addressing the temperature transferability of structure based coarse graining models," Phys. Chem. Chem. Phys. **20**, 6617–6628 (2018).

[105]T. Murtola, M. Karttunen, and I. Vattulainen, "Systematic coarse graining from structure using internal states: Application to phospholipid/cholesterol bilayer," J. Chem. Phys. **131**, 055101 (2009).

[106]J. F. Dama, A. V. Sinitskiy, M. McCullagh, J. Weare, B. Roux, A. R. Dinner, and G. A. Voth, "The theory of ultra-coarse-graining. 1. general principles," J. Chem. Theory Comput. **9**, 2466–80 (2013), http://pubs.acs.org/doi/pdf/10.1021/ct4000444.

[107]P. Kar and M. Feig, "Chapter five - recent advances in transferable coarse-grained modeling of proteins," in Biomolecular Modelling and Simulations, Advances in Protein Chemistry and Structural Biology, Vol. 96, edited by T. Karabencheva-Christova (Academic Press, 2014) pp. 143 – 180.

[108]J. R. Elliott, "Lessons learned from theory and simulation of step potentials," Fluid Phase Equilib. **416**, 27 – 41 (2016).

[109]P. Espanol, "Dissipative particle dynamics with energy conservation," Europhys. Lett. **40**, 631 (1997).

[110]P. Español, M. Serrano, I. Pagonabarraga, and I. Zúñiga, "Energy-conserving coarse-graining of complex molecules," Soft Matter **12**, 4821–4837 (2016).

[111]A. Davtyan, J. F. Dama, G. A. Voth, and H. C. Andersen, "Dynamic force matching: A method for constructing dynamical coarse-grained models with realistic time depen-

dence," J. Chem. Phys. **142**, 154104 (2015).

[112]Z. Li, H. S. Lee, E. Darve, and G. E. Karniadakis, "Computing the non-Markovian coarse-grained interactions derived from the Mori - Zwanzig formalism in molecular systems: Application to polymer melts," J. Chem. Phys. **146**, 014104 (2017), https://doi.org/10.1063/1.4973347.

TABLES

Table I. State points employed in determining the temperature- and density-dependence of CG potentials. We present the simulated ensemble and temperature, T, (in units of K), pressure, P, (in units of bar), and density, ρ, (in units of g/L). For simulations at constant volume and pressure, we present the mean internal pressure and density, respectively, observed in AA simulations.

Ethane				Methanol			
Ensemble	T	P	ρ	Ensemble	T	P	ρ
NVT	100	-868	618.7	NVT	200	-1038	792.3
NVT	125	-187	618.7	NVT	225	-880.	792.3
NVT	150	470.	618.7	NVT	250	-502	792.3
NVT	175	1078	618.7	NVT	275	-148	792.3
				NVT	300	217	792.3
NPT	100	1	661.78	NPT	200	1	883.24
NPT	125	1	628.16	NPT	225	1	856.50
NPT	150	1	593.49	NPT	250	1	829.92
NPT	175	1	556.92	NPT	275	1	803.04
				NPT	300	1	774.74

Table II. Linear fits to optimized pressure-matching coefficients: $\psi = aT + b$, where a and b are presented in units of kJ mol^{-1} K^{-1} and kJ mol^{-1} respectively, while R^2 quantifies the quality of the linear fit.

ψ	Molecule	a	b	R^2
ψ_1	Ethane	-0.30329	59.936	0.9776
ψ_1	Methanol	-0.06655	35.142	0.9873
ψ_2	Ethane	-0.04867	5.5140	0.3925
ψ_2	Methanol	-0.04277	12.913	0.3479

FIGURES

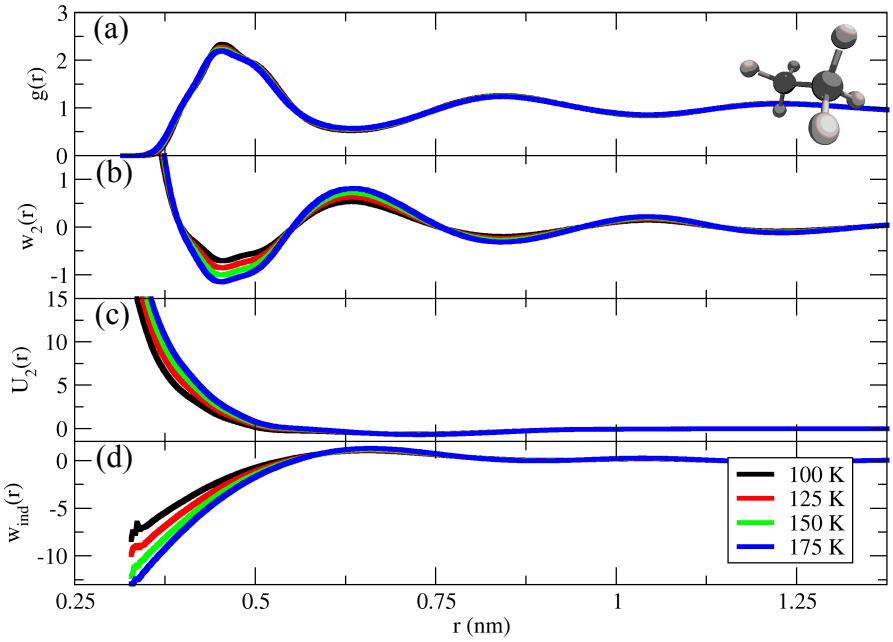

Figure 1. Pair structure and interaction potentials calculated from AA simulations in the constant NVT ensemble at a density $\rho_0 = 618.7$ g/L for a 1-site CG representation of ethane: (a) rdfs, (b) pair pmfs, (c) MS-CG pair potentials, and (d) indirect contributions to the pair pmf. Potentials are presented in units of kJ/mol. Black, red, green, and blue curves present results calculated at 100 K, 125 K, 150 K, and 175 K. The inset in panel (a) presents an ethane molecule in atomic detail with a ball-and-stick representation.

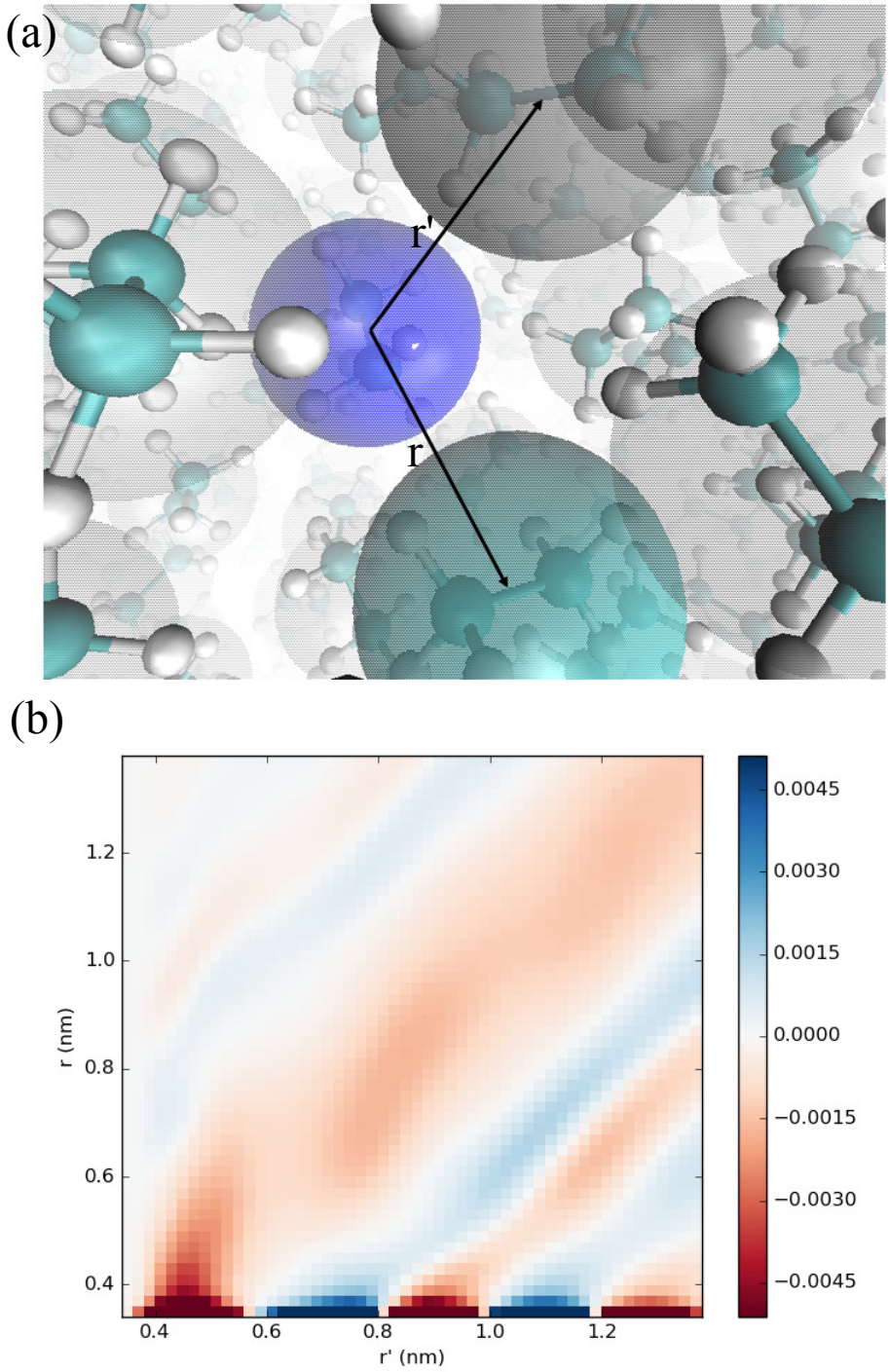

Figure 2. Three-body correlations relevant for the MS-CG pair potentials. Panel (a) indicates the geometry of solvation forces acting on a central molecule (highlighted in dark blue) in the presence of a second molecule (cyan) separated by a distance r. The third highlighted molecule (dark gray) separated by a distance r' is representative of the surrounding $N-2$ molecules (light gray) that contribute to w_{ind}. Panel (b) presents an intensity plot of the function $K(r,r')$ calculated for the 1-site representation of ethane at 150 K and constant density ρ_0.

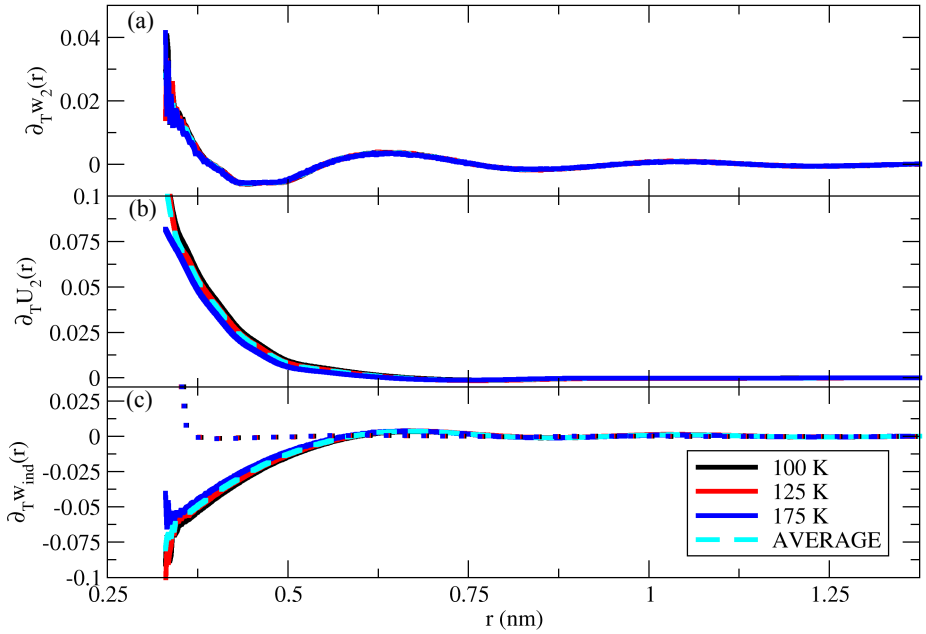

Figure 3. Finite differences quantifying the temperature variation (at constant density) in the pair structure and interaction potentials for a 1-site CG representation of ethane: (a) pair pmfs, (b) MS-CG pair potentials, and (c) indirect contributions to the pair pmf. Finite differences are presented in units of kJ/(mol K). Black, red, and blue curves present results calculated with $T =$ 100 K, 125 K, and 175 K, respectively. The dashed cyan lines represent the average of the three finite differences, while the dotted curves in panel (c) present contributions arising from $\partial_T K$.

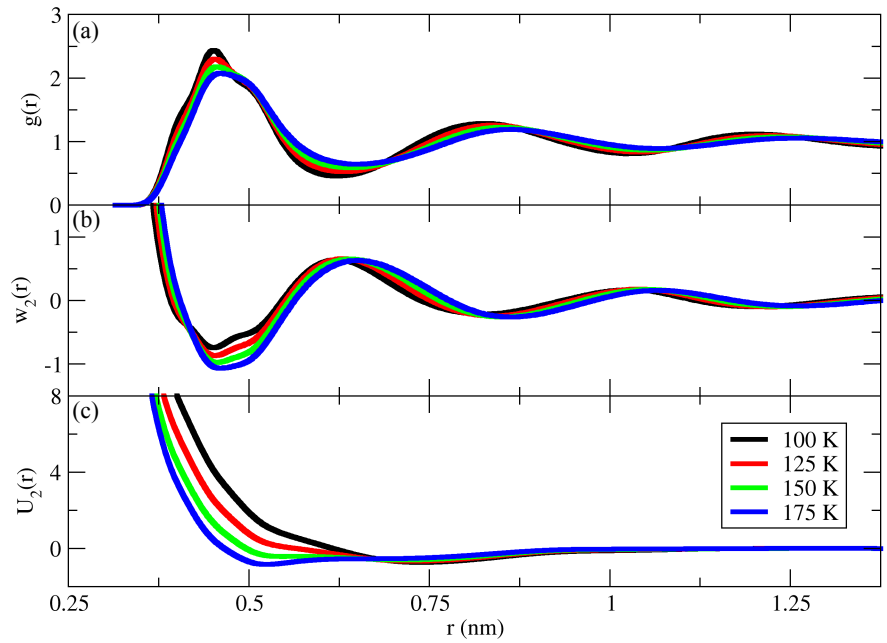

Figure 4. Pair structure and interaction potentials calculated from AA simulations in the constant NPT ensemble at $P_0 = 1$ bar external pressure for a 1-site CG representation of ethane: (a) rdfs, (b) pair pmfs, and (c) MS-CG pair potentials. Potentials are presented in units of kJ/mol. Black, red, green, and blue curves present results calculated at 100 K, 125 K, 150 K, and 175 K.

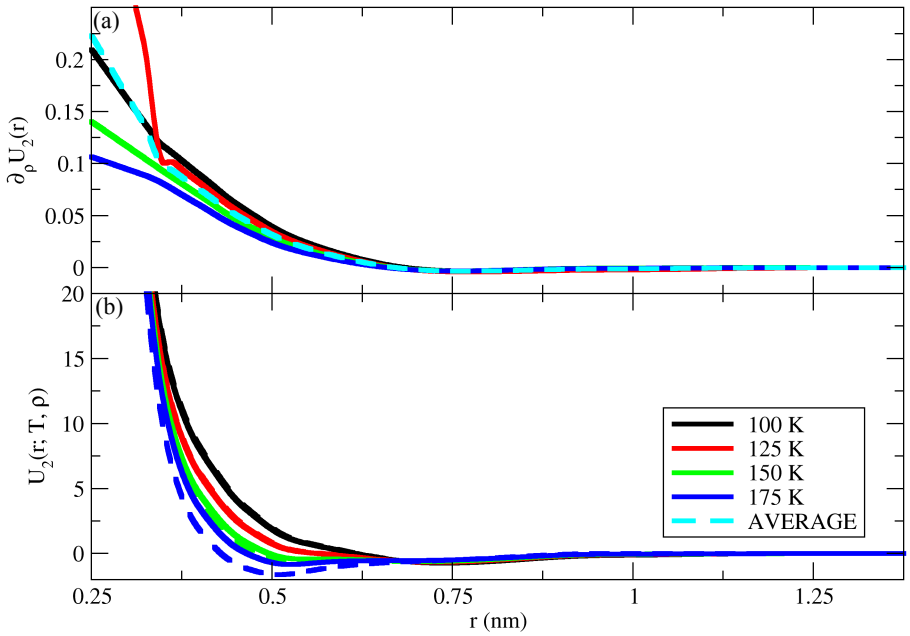

Figure 5. (a) Finite differences quantifying the density variation (at constant temperature) in the MS-CG pair potentials for a 1-site CG representation of ethane. (b) Comparison of MS-CG potentials calculated at constant external pressure (solid curves) and potentials obtained via linear extrapolation from potentials calculated at constant density (dashed curves). Potentials are presented in units of kJ/mol, while finite differences are presented in units of kJ/(mol (g/L)). Black, red, green, and blue curves present results calculated at 100 K, 125 K, 150 K, and 175 K. The dashed cyan line in panel (a) represents the average of the finite differences calculated for the 4 temperatures.

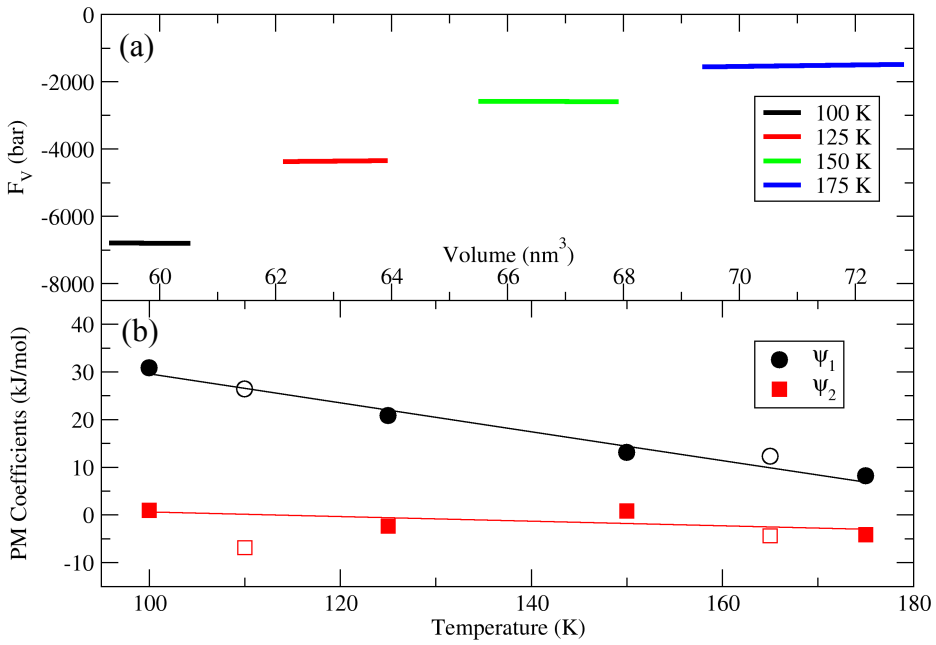

Figure 6. Volume forces (a) and pressure matching coefficients (b) for 1-site CG models of ethane. In panel (a) the black, red, green, and blue curves present volume forces optimized for 1 bar external pressure and temperatures T = 100 K, 125 K, 150 K, and 175 K. The length of each line spans three standard deviations in the volume distribution about the average volume. In panel (b), the symbols indicate coefficients optimized for constant NPT simulations at 1 bar external pressure and the specified temperatures. The lines represent the best fit to the coefficients indicated by the solid symbols. The open symbols indicate optimized parameters at additional temperatures T = 110 K and 165 K that were not employed in determining the linear fit.

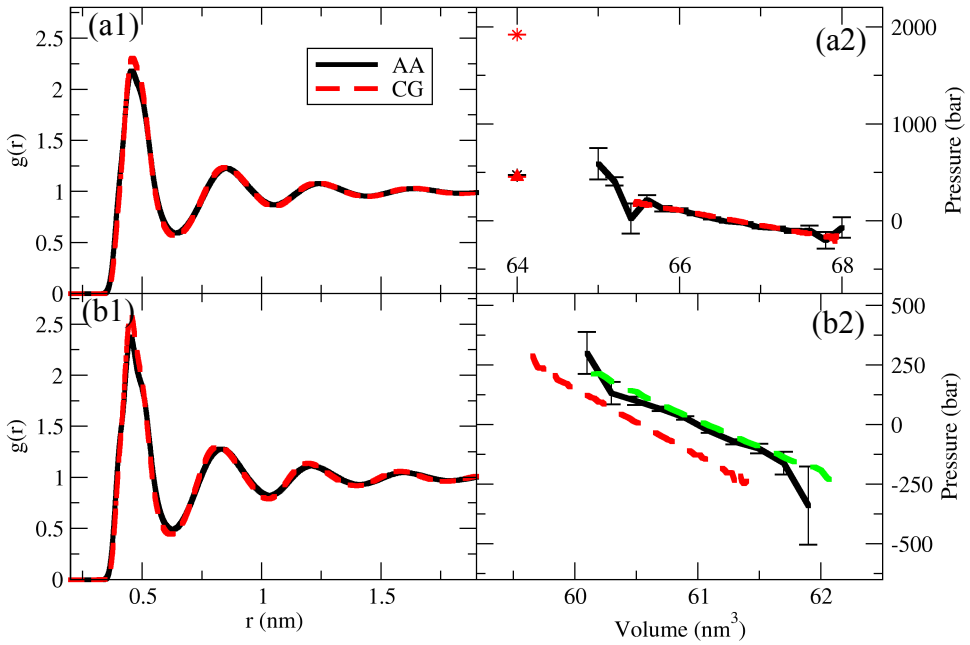

Figure 7. Comparison of the rdfs (left) and average pressures (right) obtained from constant NPT simulations of AA and CG models for ethane at 1 bar external pressure. The top and bottom rows present results from simulations at $T = 150$ K and 110 K, respectively. In the top row, the dashed red curves present results for CG potentials parameterized for the specified state point. In the bottom row, the dashed red curves present results for CG potentials predicted by linear extrapolation, while the green curve presents results after further refining the volume potential. Additionally, the isolated black and red points in panel (a2) present the volume and average pressure for AA and CG simulations, respectively, in the constant NVT ensemble at the temperature $T = 150$ K with the constant density $\rho_0 = 618.7$ g/L.

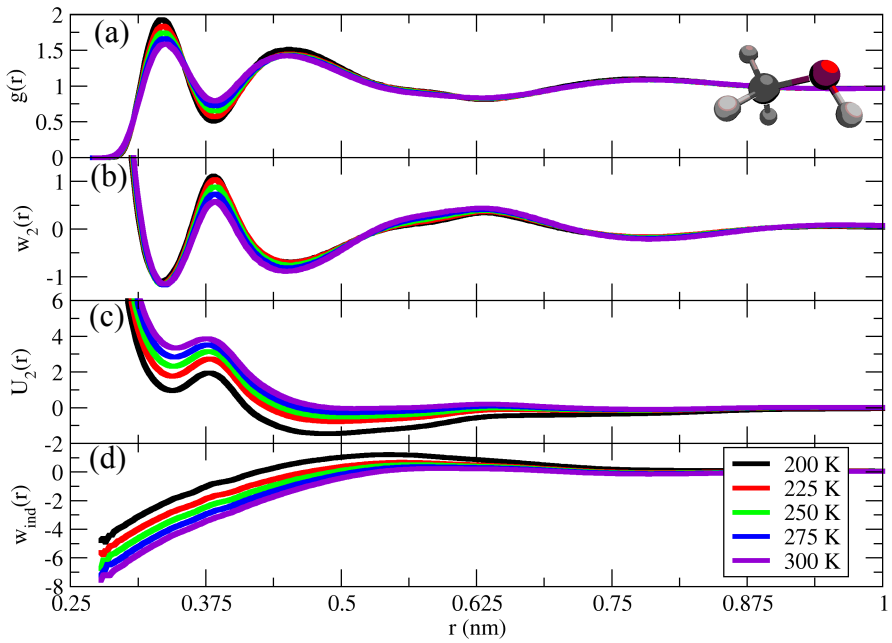

Figure 8. Pair structure and interaction potentials calculated from AA simulations in the constant NVT ensemble at a density $\rho_0 = 792.3$ g/L for a 1-site CG representation of methanol: (a) rdfs, (b) pair pmfs, (c) MS-CG pair potentials, and (d) indirect contributions to the pair pmf. Potentials are presented in units of kJ/mol. Black, red, green, blue, and purple curves present results calculated at 200 K, 225 K, 250 K, 275 K, and 300 K. The inset in panel (a) presents a methanol molecule in atomic detail with a ball-and-stick representation.

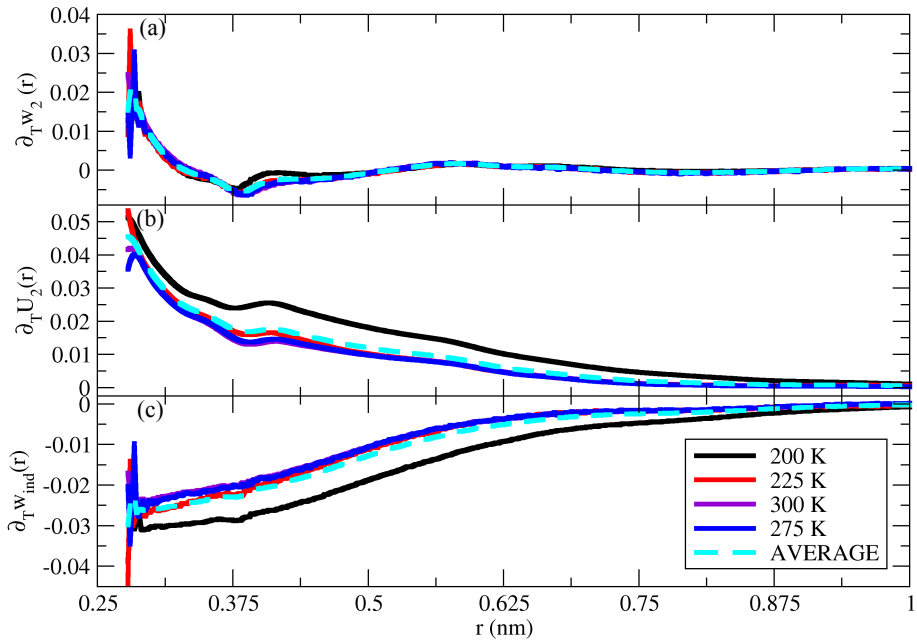

Figure 9. Finite differences quantifying the temperature variation (at constant density) in the pair structure and interaction potentials for a 1-site CG representation of methanol: (a) pair pmfs, (b) MS-CG pair potentials, and (c) indirect contributions to the pair pmf. Finite differences are presented in units of kJ/(mol K). Black, red, blue, and purple curves present results calculated with T = 200 K, 225 K, 275 K, and 300 K, respectively. The dashed cyan lines present averages of the four finite differences.

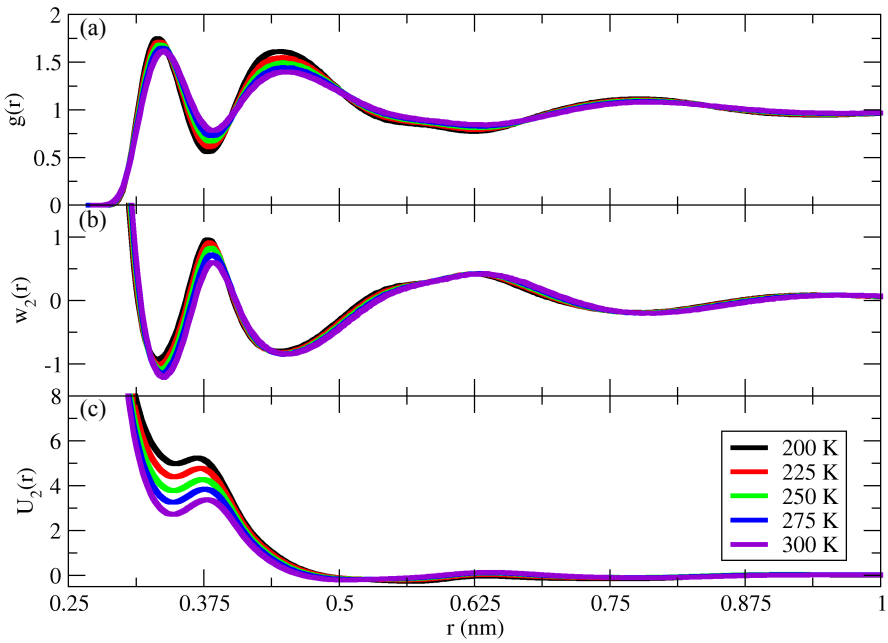

Figure 10. Pair structure and interaction potentials calculated from AA simulations in the constant NPT ensemble at $P_0 = 1$ bar external pressure for a 1-site CG representation of methanol: (a) rdfs, (b) pair pmfs, and (c) MS-CG pair potentials. Potentials are presented in units of kJ/mol. Black, red, green, blue, and purple curves present results calculated at 200 K, 225 K, 250 K, 275 K, and 300 K.

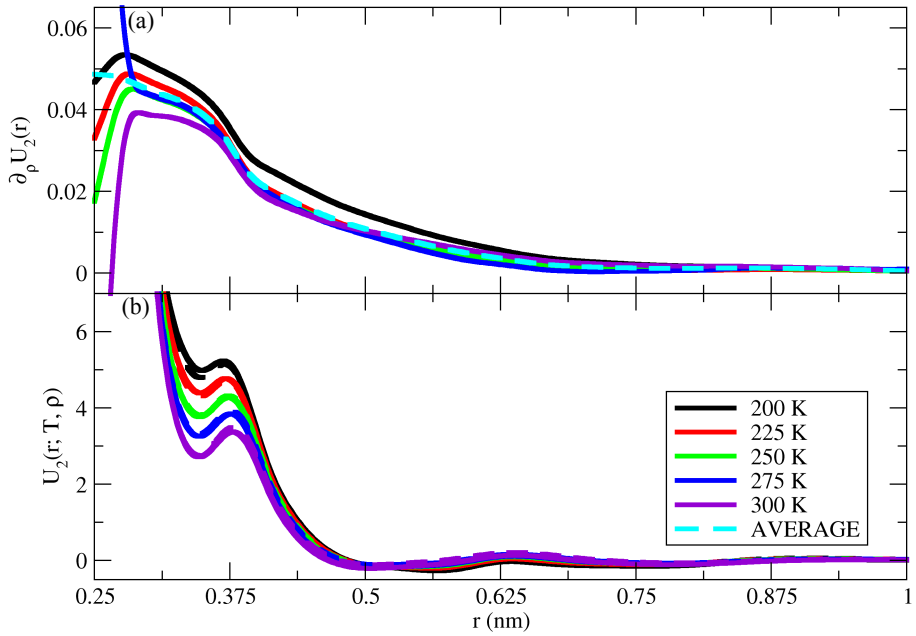

Figure 11. (a) Finite differences quantifying the density variation (at constant temperature) in the MS-CG pair potentials for a 1-site CG representation of methanol. (b) Comparison of MS-CG potentials calculated at constant external pressure (solid curves) and potentials obtained via linear extrapolation from potentials at constant density (dashed curves). Potentials are presented in units of kJ/mol, while finite differences are presented in units of kJ/(mol (g/L)). Black, red, green, blue, and purple curves present results calculated at 200 K, 225 K, 250 K, 275 K, and 300 K. The dashed cyan line in panel (a) presents the average of the finite differences calculated for the 5 temperatures.

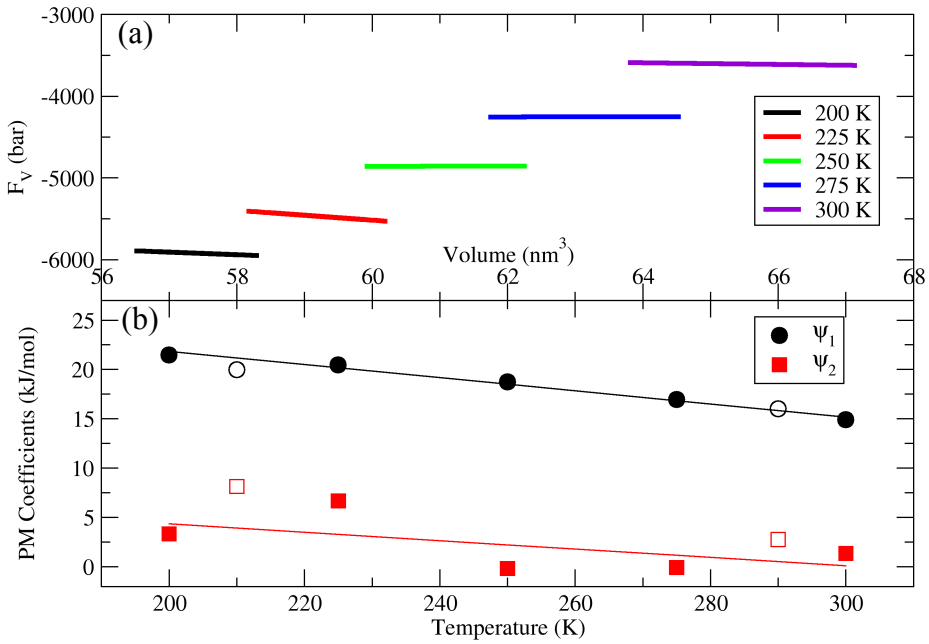

Figure 12. Volume forces (a) and pressure matching coefficients (b) for 1-site CG models of methanol. In panel (a) the black, red, green, blue, and purple curves present volume forces optimized for 1 bar external pressure and temperatures T = 200 K, 225 K, 250 K, 275 K, and 300 K. The length of each line spans three standard deviations in the volume distribution about the average volume. In panel (b), the symbols indicate coefficients optimized for constant NPT simulations at 1 bar external pressure and the specified temperatures. The lines represent the best fit to the coefficients indicated by the solid symbols. The open symbols indicate optimized parameters at additional temperatures T = 210 K and 290 K that were not employed in determining the linear fit.

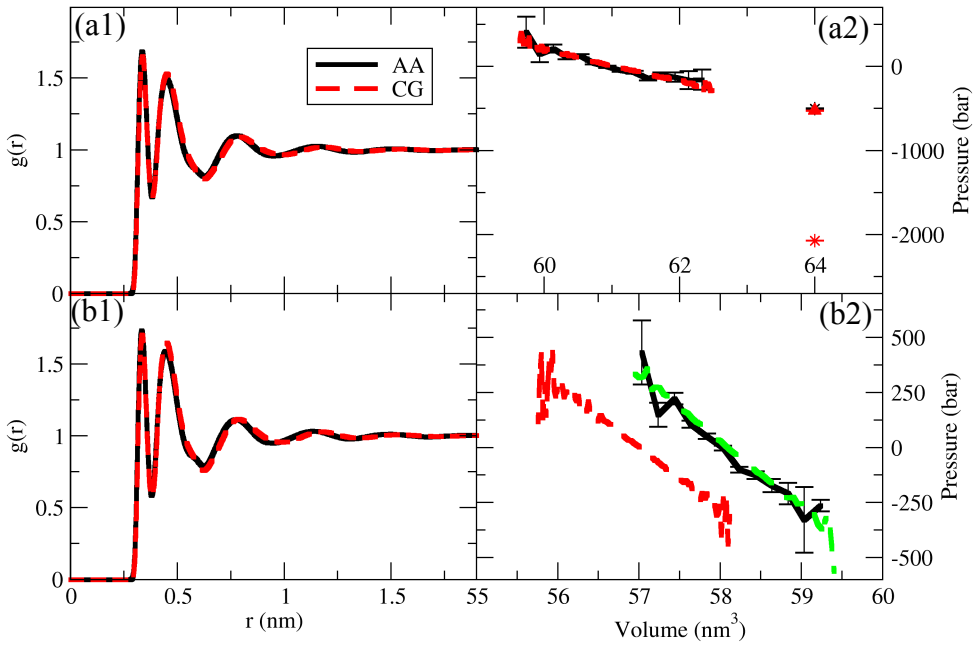

Figure 13. Comparison of the rdfs (left) and average pressures (right) obtained from constant NPT simulations of AA and CG models for methanol at 1 bar external pressure. The top (a) and bottom (b) rows present results from simulations at $T = 250$ K and at 210 K, respectively. In the top row, the dashed red curves present results for CG potentials parameterized for the specified state point. In the bottom row, the dashed red curves present results for CG potentials predicted by linear extrapolation, while the green curve presents results after further refining the volume potential. Additionally, the isolated black and red points in panel in panel (a2) present the volume and average pressure of AA and CG simulations, respectively, in the constant NVT ensemble at the temperature $T = 250$ K with the constant density $\rho_0 = 792.3$ g/L.